applied sciences

MDPI

*Article*

# Behavior of Confined Headed Bar Connection for Precast Reinforced Concrete Member Assembly

**Zihao Liang [1], Chao Gong [2], Weiqiao Liang [3], Sumei Zhang [1,*] and Xiaozhong Li [1]**

[1] School of Civil and Environmental Engineering, Harbin Institute of Technology, University Town, Shenzhen 518055, China
[2] Central Research Institute of Building and Construction Co., Ltd., MCC, No. 33, Xitucheng Road, Beijing 100088, China
[3] China Minmetals Corporation, Tower A Minmetals Plaza, No. 3, Chao Yangmen North Avenue, Dongcheng District, Beijing 100010, China
* Correspondence: smzhang@hit.edu.cn

**Abstract:** The mechanical performance of precast RC structures relies on the connections, especially the connections of steel bars, between precast RC members. Grouted sleeve splices and grouted spiral-confined overlap connections are widely used in engineering practice in China. Both of these two connection splices require on-site grouting. The process is concealed and invisible, leading to difficult on-site inspection. The unseen defects cause a challenge for detection and repair, which may impair the reliability of precast RC members' behavior. This paper presents an RC member assembly connection with visible on-site construction quality-monitoring. The proposed confined headed-bar connection (CHBC) consists of two overlapping headed bars and confinement stirrup. With CHBC, the potential construction defects are diminished, and subsequently the construction quality as well as the reliability is upgraded. Experimental investigation on 18 CHBC specimens was carried out; the main parameters considered were overlap length and bar-head size. The failure modes, bearing capacity, stirrup strain development and bond versus slip response are studied. Working mechanism of CHBC is investigated in terms of bond behavior force and concrete compression force at head experimentally and numerically; distributive relationship of these two forces is revealed. The results show that for Φ12 reinforcement, a 90 mm overlap length under test parameters is adequate to reach headed bar ultimate strength in CHBC. Finally, a CHBC-bearing capacity prediction method is suggested based on the superposition method and strut-and-tie model theory.

**Keywords:** connection splice; headed bar; overlap length; strut-and-tie model; bearing capacity

check for updates

**Citation:** Liang, Z.; Gong, C.; Liang, W.; Zhang, S.; Li, X. Behavior of Confined Headed Bar Connection for Precast Reinforced Concrete Member Assembly. *Appl. Sci.* **2023**, *13*, 827. https://doi.org/10.3390/app13020827

Academic Editor: Alexey Beskopylny

Received: 13 December 2022
Revised: 29 December 2022
Accepted: 2 January 2023
Published: 6 January 2023

**Copyright:** © 2023 by the authors. Licensee MDPI, Basel, Switzerland. This article is an open access article distributed under the terms and conditions of the Creative Commons Attribution (CC BY) license (https://creativecommons.org/licenses/by/4.0/).

## 1. Introduction

The precast concrete structure has attracted spectacular attention in the engineering field for its high quality, low cost, high construction speed and low carbon emission characteristics [1–3]. Manufactured in the factory, the precast concrete elements are assembled on site after the transportation. The industrialization ensures the quality of the element itself but the connection among different elements in situ affects the performance of the overall structure. Thus, the connections become the key to ensure the precast structure being of a high quality. The connections in precast concrete structure can be multiple, and in most cases, the connection of the steel bars is significantly important.

Different methods have been advanced to process the connection of steel bars. In the late 1960s, Alfred A. Yee proposed the grouted sleeve-splice connection [4]. Ever since that, numerous pieces of research have been conducted. The mechanical performance of grouted sleeve splice under monotonic [5–9] and cyclic [10–12] loading have been conducted through experimental and numerical investigations. In addition, the mechanical performance of precast concrete members connected by a grouted sleeve splice including a shear wall [13–15] and a column [16–19] are studied and the results demonstrate that

the structural members with grouted sleeve splice show as good a structural performance as those cast-in-place. Apart from grouted sleeve splice, Jiang [20] proposes the grouted spiral-confined lap connection and applies it to the steel bar connection of the precast shear wall [21,22] and beam-column-slab joints [23]. Through experimental and numerical investigations, the structural reliability of such a connection is proved. It should be noted that the grouted sleeve splice connection and grouted spiral-confined lap connection are the most widely used connection methods in the Chinese engineering field. However, these two methods may be disadvantageous in some cases.

Grouting is needed either for grouted sleeve splice or grouted spiral-confined lap connection and it is a type of concealed construction process for which the construction process cannot be supervised directly and visibly. The difficult on-site inspection can result in poor construction quality as well as grouting defects. Through experimental investigations, reduction in the tensile capacity of grouted sleeve splice due to grouting defects has been validated [24,25]. Additionally, Xiao [26] discovered that the defects can post adverse effects on the mechanical performance of the overall precast concrete shear wall including the bearing capacity dropping by 32% and the energy dissipation decreasing by 35% compared with the non-defect shear wall. Reduction effects can be also observed for the precast column connected by a defective grouted sleeve splice [27,28]. Although several methods have been proposed to detect the grouting defects such as the impact-echo method, X-ray method, damping vibration method and so on, these methods need embedded sensors or specific testing instruments with the assistance of professionals, which causes inconvenience and increases the costs during construction. Additionally, even if the defects are detected, it is difficult to repair the defects with the structures being undamaged. Overall, the unseen defects cause a challenge for detection and repair, which may impair the reliability of precast RC member behavior. Apart from the grouting defects, the construction speed of the grouted sleeve splice or grouted spiral-confined lap connection can be limited by a low construction error tolerance. The on-site connection of precast concrete members needs the lifting of, then placing the concrete members into the design position. For grouted sleeve splice or grouted spiral-confined lap connection, after lifting, the steel bars in the precast member need to plug into the sleeve or grouting holes of another precast member and this inserting process requires a high degree of accuracy in geometry. For example, the error tolerance of insertion for grouted sleeve splice is generally about 10 mm to 15 mm. The construction can be inconvenient and time-consuming due to the required high construction accuracy which slows down the construction speed. The unseen grouting defects and required high construction accuracy of grouted sleeve splice or grouted spiral-confined lap connection violate the advantages of high construction quality and speed for precast concrete structure. Considering the deficiencies of the existing connection splices and the in-situ construction situations, this paper proposes a new steel-bar connection splice named as confined headed bar connection (CHBC) as shown in Figure 1.

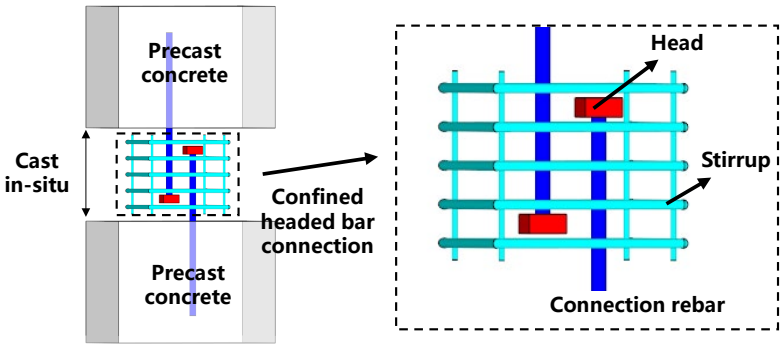


**Figure 1.** Confined headed bar connection (CHBC).

As shown in Figure 1, CHBC consists of two overlapped headed bars and confinement stirrup. With CHBC, the cast-on-site construction is adopted instead of concealed grouting. Once the headed bar and stirrup reinforcement is placed, the reinforcement connection can be achieved after the connection area is cast-on-site. The CHBC construction process can be monitored visibly while the potential construction defects are diminished, and subsequently the construction quality as well as the reliability is upgraded. Additionally, the construction error tolerance is improved since the steel bar is not needed anymore to plug into the sleeve or grouting hole. The performance of the steel bar splice in concrete is strongly related to the anchorage properties of the steel bar. The stirrup confining the concrete at lap region can improve the rebar anchorage performance and furthermore, the heads at the end of the rebars can greatly strengthen the anchorage capacities. Through push-out tests, researchers [29–35] have found that the headed bar can achieve design tensile strength with significantly less embedded length compared to straight rebars without heads. The headed bars are also effective in the beam–column joint connection which can reduce the anchorage length of beam rebars in the column region [36]. Different design codes also quantify the improvement by head. Chinese design code GB 50010-2020 [37] suggests 40% off for the anchorage length of the headed bar while American design specification ACI318-19 [38] suggests the minimum anchorage length of the headed bar can be about 0.4 times that of the straight bar with specific conditions. In addition, researchers have adopted the headed-bar overlap splice to connect the steel bars between precast concrete members such as beam and slab [39–44]. Results show that the precast concrete members connected by headed-bar overlap splice show practical and good bearing capacities and deformation characteristics when compared to those of continuous steel bars. The headed-bar overlap splice is practical for precast reinforced concrete member assembly.

Although the feasibility of the lap-headed bar has been proved, the characteristics such as ultimate strength, slip behavior between the steel bar and concrete and so on, of this kind of steel bar connector has scarcely been studied. Moreover, the improvement added by the additional stirrup has not been investigated. So, in this paper, an experimental investigation including 18 specimens with different lap lengths and head sizes has been conducted to study the mechanical performance of CHBC under tension. The discussion is focused on the failure modes, bearing capacities and stirrup strain development, etc. The bearing capacity of CHBC consists of bond behavior force and concrete compression force at the head. The distributive relationship of these two forces has been investigated. In addition, the load–slip response of CHBC is studied. Moreover, an advanced finite element model using ABAQUS has been established, providing access to the detailed investigation of the mechanisms for concrete compression at head. Finally, based on the superposition method and strut-and-tie model (STM) theory, a prediction method to determine the bearing capacity of CHBC has been suggested. Apart from that, the calculation of the required head thickness is suggested to prevent the head from yielding. The proposed CHBC can offer the engineers a new option in the design of steel bar connection in the precast concrete structure. The analytical results can provide a theoretical basis for the generalization of CHBC.

## 2. Experimental Program

### *2.1. Specimen Design and Preparation*

The specimen layout (Figure 2) referred to in the Vieito study [45] was adopted. The PVC tube was used to debond the rebar within the concrete cover region. Additionally, it can be seen that four headed bars were arranged inside one single specimen to achieve the symmetrical configuration. If two headed bars were placed, then it was impossible to achieve the symmetrical configuration and therefore, the specimen rotated unavoidably when the tensile load was applied. Furthermore, when CHBC was applied in the connection of precast concrete structure, the symmetrical configuration was easily achieved.

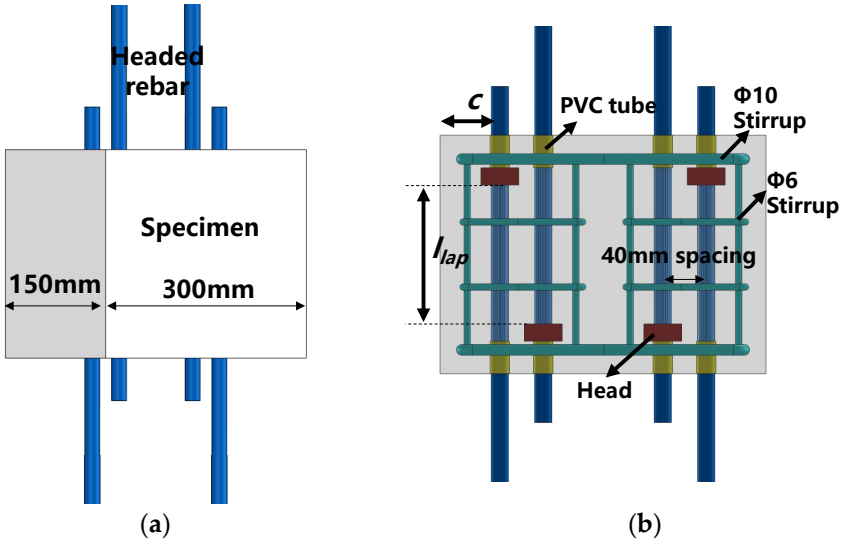


**Figure 2.** Sketch of the specimen (**a**) Specimen layout (**b**) Layout inside the concrete.

A total of 18 specimens were designed in order to investigate the mechanical performance of CHBC. The variables considered in this study included head size and lap length. Details of the 18 specimens can be seen in Table 1, where $a_h$ is the side length of the square head; $d$ is the diameter of headed bar; $A_h$ denotes the surface area of head and $A_s$ denotes the cross-sectional area of headed bar; $l_{lap}$ represents the lap length as shown in Figure 2 and $c$ stands for the concrete cover thickness for headed bar. It should be noted that the lap length of the steel bar varied from about $0.19l_l$ to $0.28l_l$, while $l_l$ was the required lap length for straight rebar in the Chinese specification GB 50010-2020 [37]. The fabrication process of the specimens can be seen in Figure 3. The specimens were naturally cured for 28 days after pouring.

**Table 1.** Details of specimens for test.

| No. | Specimen ID | $a_h$ (mm) | $d$ (mm) | $A_h/A_s$ | $l_{lap}$ (mm) | $l_{lap}/d$ | Stirrup | $c$ (mm) | Number of Specimens |
|---|---|---|---|---|---|---|---|---|---|
| 1 | M4-D12-6d | 22 | 12 | 4.0 | 72 | 6 | Φ6@40 | 49 | 3 |
| 2 | M4-D12-7.5d | 22 | | 4.0 | 90 | 7.5 | | | 3 |
| 3 | M4-D12-9d | 22 | | 4.0 | 108 | 9 | | | 3 |
| 4 | M3-D12-7.5d | 18 | | 3.0 | 90 | 7.5 | | | 3 |
| 5 | M6-D12-7.5d | 26 | | 6.0 | 90 | 7.5 | | | 3 |
| 6 | M8-D12-7.5d | 30 | | 8.0 | 90 | 7.5 | | | 3 |

Note: In the label of "M4-D12-6d", "M4" represents that the value of head surface area divided by the headed steel bar cross-sectional area is equal to 4; "D12" represents the diameter of the headed steel bar is equal to 12 mm; "6d" represents the value of lap length divided by the diameter of the headed steel bar is equal to 6.


**Figure 3.** *Cont.*

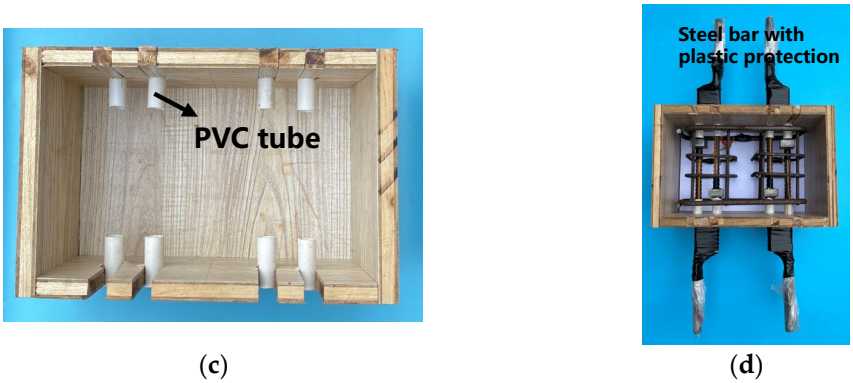


**Figure 3.** Production of specimens (**a**) Steel bar with head plate; (**b**) Strain gauge operation; (**c**) Mold; (**d**) Fabricated specimen.

### *2.2. Test Setup and Loading Scheme*

Specimens were placed on a specific load frame where the headed rebars were clamped to the reaction platens of the load frame (Figure 4). Tensile force from the universal testing machine was applied to the specimens through the load frame. The tensile loading was firstly applied to the specimen by the force control manner of 0.3 kN/s and after the steel bar yielding, it was controlled by the displacement manner of 1 mm/min. It should be noted that levering and centering of the testing sample was conducted and preloading was also accomplished to ensure the tension force from the universal testing machine could apply homogeneously to all the headed bars from the very beginning of the test.

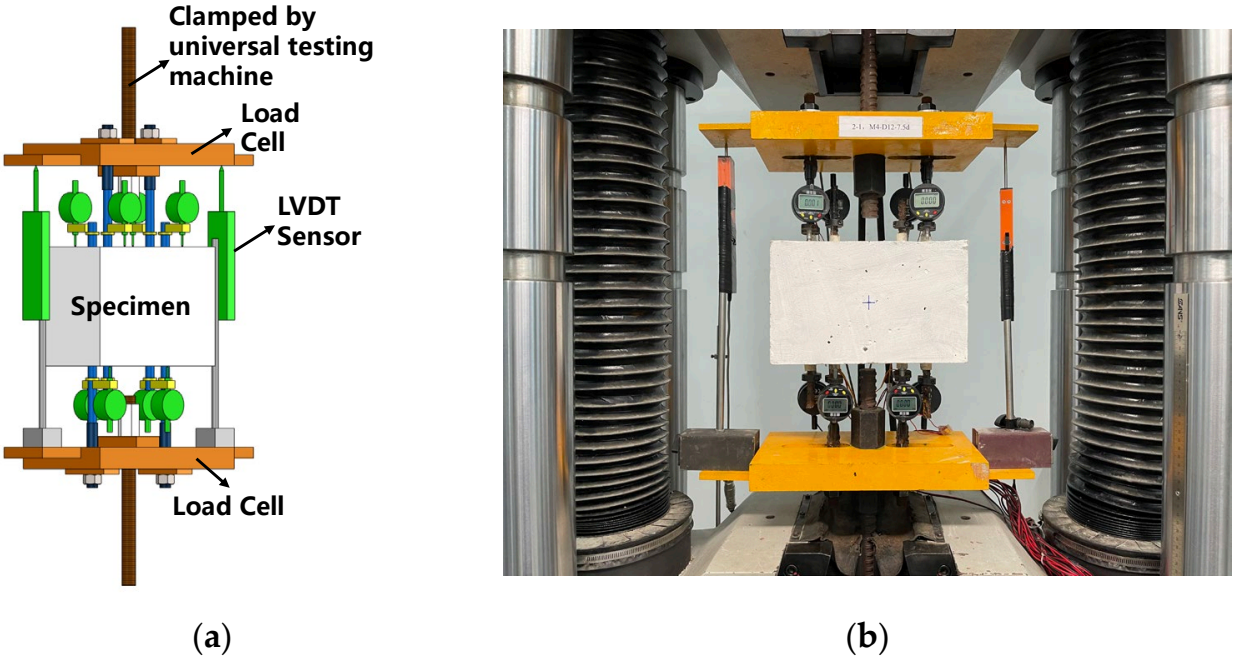


**Figure 4.** Load frame (**a**) Loading sketch; (**b**) Load frame with a specimen settled down.

During the test, displacement transducers (LVDTs) were employed to measure the axial deformation of CHBC (Figure 4). Additionally, micrometer calipers were used to observe the slip between the headed rebar and concrete (Figure 5a). In addition, strain gauges were placed on the headed bars and stirrups, respectively, (Figure 5b) to detect the strain development.

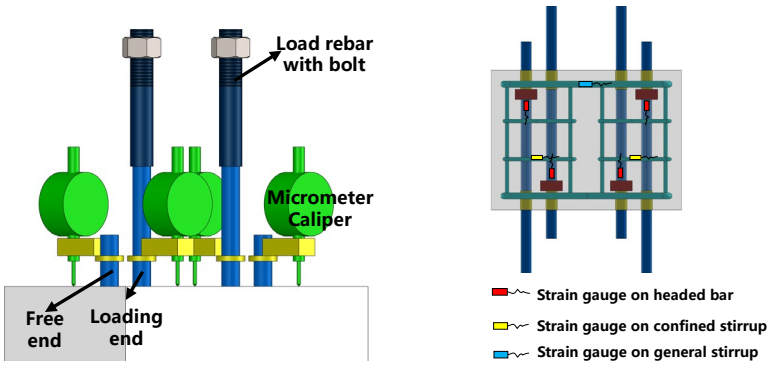


**Figure 5.** Measurement system (**a**) Measurement of slip; (**b**) Strain gauge layout.

### *2.3. Materials*

In this study, the concrete and steel reinforcement are commercially available. The heads were shaped from profile steel plate of 16 mm thickness and the steel bars were hot-rolled ribbed bars with nominal yield strength of 400 MPa (HRB400). The concrete material tests were conducted according to Chinese specification GB/T 50081-2019 [46] and the steel materials' tests referred to the Chinese standard GB/T 28900-2012 [47] and GB/T 228.1-2021 [48] for steel bar and head, respectively. The test results can be seen in Table 2. The denotation $f_{cu}$ and $f_c$ are the cubic and prismatic strength of the concrete, respectively. $f_y$ represents the yield strength of the steel materials while $f_u$ represents the ultimate tensile strength. $E_c$ and $E_s$ are the elastic modulus of concrete and steel materials, respectively, and $v$ is the Poisson's ratio. Mixture ratio of the commercial concrete used can be seen in Table 3.

**Table 2.** Mechanical properties of concrete and steel.

| Material | $f_{cu}$ (MPa) | $f_c$ (MPa) | $f_y$ (MPa) | $f_u$ (MPa) | $E_c$ or $E_s$ (GPa) | $v$ |
|---|---|---|---|---|---|---|
| C30 concrete | 31.9 | 19.7 | / | / | 28.9 | 0.212 |
| Φ6 stirrup | / | / | 463.4 | 613.7 | 209.2 | / |
| Φ10 stirrup | / | / | 472.5 | 637.0 | 195.4 | / |
| Φ12 headed bar | / | / | 448.6 | 617.2 | 199.0 | / |
| Head steel plate | / | / | 250.7 | 407.3 | 209.3 | 0.282 |

**Table 3.** Concrete mixture ratio.

| Grade | Water to Binder Ratio | Water (kg/m$^3$) | Cement (kg/m$^3$) | Fine Aggregate (kg/m$^3$) | Coarse Aggregate (kg/m$^3$) | Superplasticizer (kg/m$^3$) | Fly Ash (kg/m$^3$) |
|---|---|---|---|---|---|---|---|
| C30 | 0.40 | 153 | 300 | 710 | 1110 | 7.6 | 80 |

## 3. Experimental Results

### *3.1. Overall Behavior and Failure Modes*

The failure modes of all the specimens can be classified into two types. One is the steel bar connector failure and the other is steel bar rupture failure.

For the specimens of steel bar connector failure, take specimen M4-D12-7.5d (No. 2 specimen) as an example. At the early stage of loading, few visible cracks are generated at the concrete surface and the specimens undergo the elastic deformation stage. As the load increases, the steel bars yield and the specimens change from elastic deformation stage into elastic–plastic deformation stage. After that, the diagonal cracks are generated between the two heads among all the specimens and part of the specimens generate the

horizontal cracks which develop from the edge side to the inner side of the concrete. It should be noted that the diagonal cracks may generate at a single side of the specimens and it results in the uneven bar stress among the four headed bars, which can lead to the rotation of specimens consequently. In addition, since the four headed bars cannot yield simultaneously, it can also result in uneven bar stress among the four headed bars as well as the undesirable rotation of specimens. As it reaches peak load, the diagonal and horizontal cracks are developed and the cracks are clearly visible at the concrete surface (Figure 6).

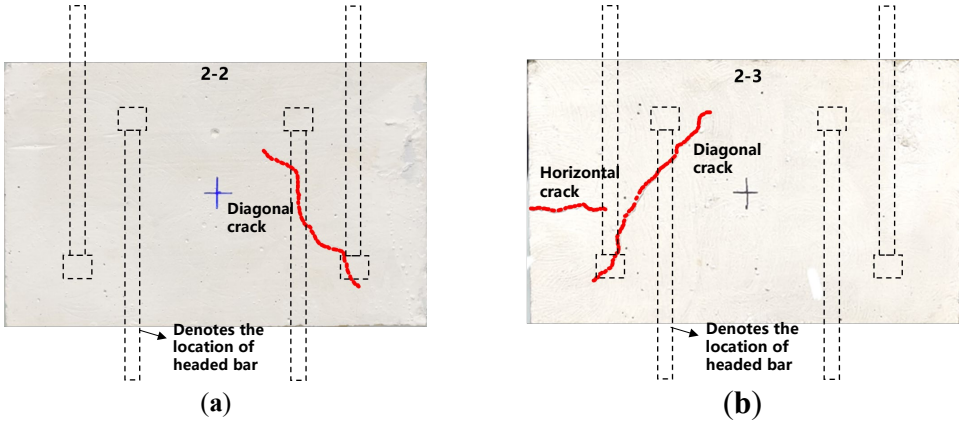


**Figure 6.** Crack development at peak load (**a**) Diagonal crack (specimen 2-2); (**b**) Horizontal crack (specimen 2-3).

During the post-peak stage, new vertical cracks are generated and they develop fast along with the rotation of the specimens becoming obvious and the stress nonuniformity of the headed bars also increases rapidly (Figure 7). Besides, for the specimens without horizontal cracks before, horizontal cracks are generated and develop fast with the increase in rotation of the specimens. It can be inferred that the horizontal cracks are generated due to the rotation of the specimens. Additionally, multiple cracks are generated and develop fast at the side of the concrete surface and eventually, the side concrete blows out. It should be noted that while CHBC is applied in the structure members such as shear walls or beams, the rotation due to the uneven bar stress is limited by the concrete and reinforcement inside the structure members and the mentioned side concrete blow-out failure can be prohibited. Loading ceases before the harmful rotation of the specimens is too large and any loading unsafety is possible.

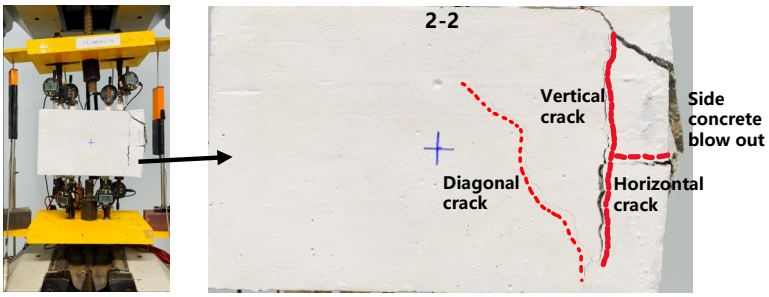


**Figure 7.** Crack development at post-peak stage.

For the specimens of steel-bar rupture failure, take specimen M8-D12-7.5d (No. 6 specimen) as an example. Similarly, few cracks generate before the headed bars are yielding. During the hardening deformation stage, diagonal cracks are observed at the concrete surface between the two heads and part of the specimens generate horizontal cracks (Figure 8). As it reaches peak load, the headed bars stresses are closed to ultimate tensile strength and one of the headed bars ruptures soon after the local necking of the steel bar is evident. It should be noted that the side concrete blow-out failure does not happen and

except for the diagonal and horizontal cracks generated initially, few cracks are developed during the whole loading process.

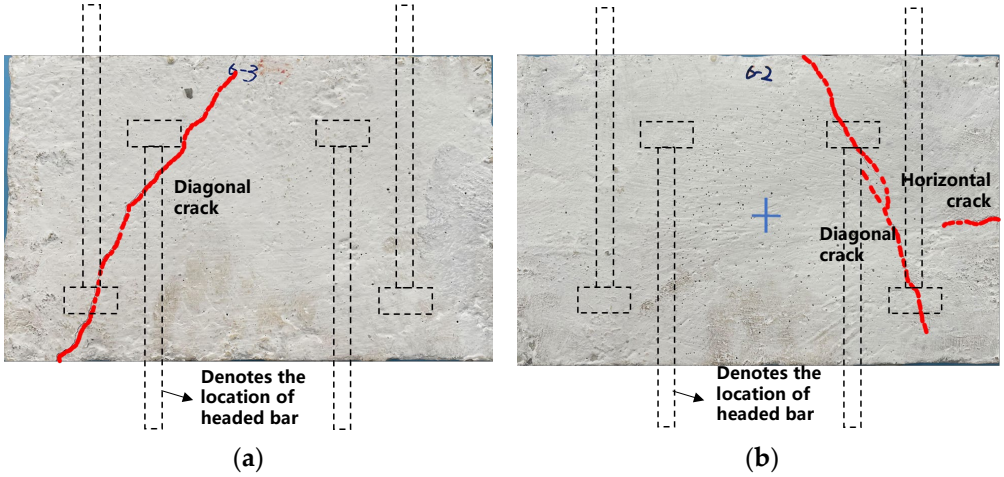


**Figure 8.** Crack development at peak load (**a**) Diagonal crack (specimen 6-3); (**b**) Horizontal crack (specimen 6-2).

In conclusion, the failure process of the specimens is divided into four stages, as shown in Figure 9. In the beginning, all the materials remain elastic while the load–displacement response is linear at this stage. As the loads increase and the headed bars yield, it enters the next stage in which plastic deformations of the headed bars are accumulated. Soon after stage two, strain hardening of the headed bars occurs. During stage three of hardening, diagonal cracks are generated with the increase in loads. Finally, the specimens achieve their bearing capacity and subsequently fail in the different modes mentioned above.

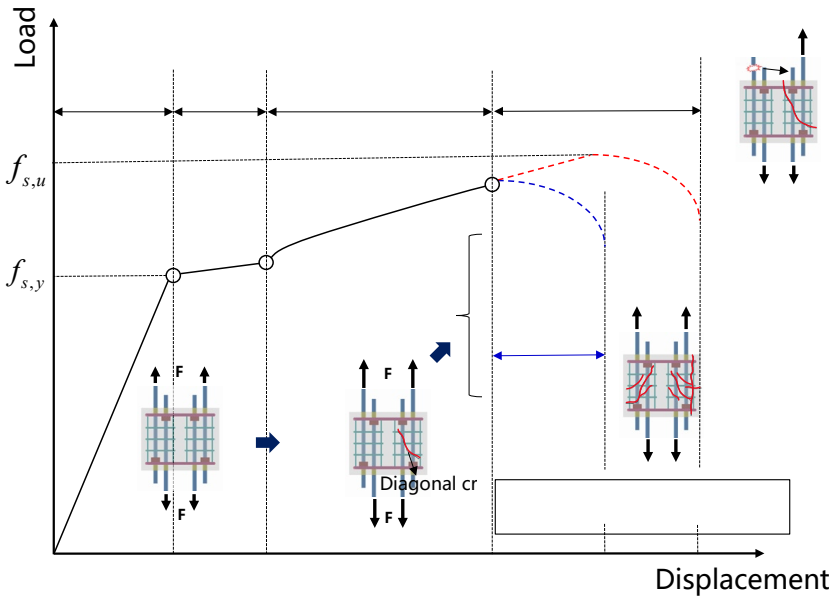


**Figure 9.** Four stages of failure process.

The summary of the crack development at peak load among all the specimens can be seen in Figure 10. It can be concluded that for all the specimens, either of steel bar connector failure or of steel bar rupture failure, diagonal cracks are observed at the concrete surface between the two heads.

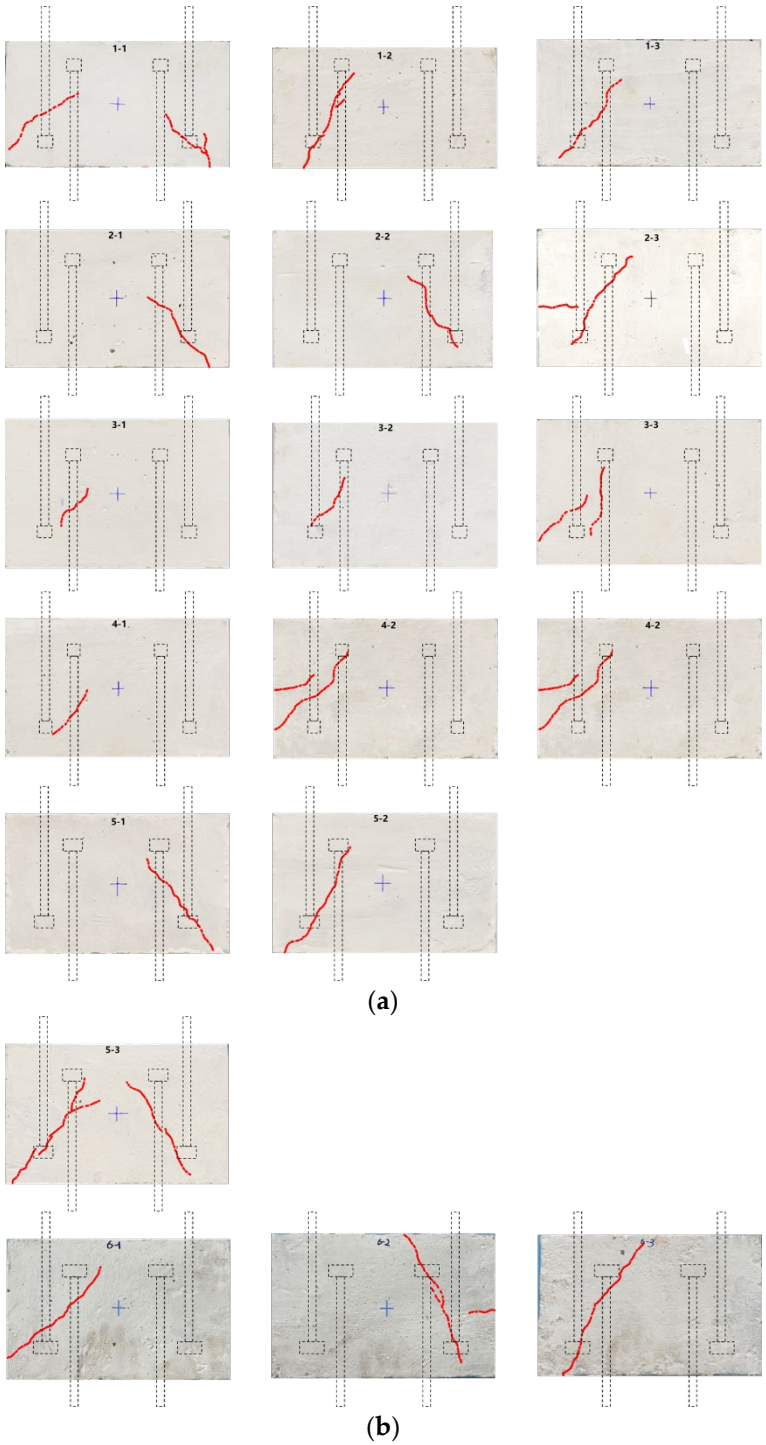


**Figure 10.** Crack development at peak load for all the specimen (**a**) Steel bar connector failure; (**b**) Steel bar rupture failure.

The diagonal cracks can be associated with the shear cracks of the reinforced concrete beam with a relatively small shear-span ratio. In the discussion of diagonal shear cracks, the strut-and-tie model (STM) can be adopted. When the concrete beam with a small shear span ratio is subjected to shear force, a diagonal concrete compression strut of bottle shape is generated between the load end and support end (Figure 11). When the compression stress in the diagonal strut is high, splitting cracks generate along the axial direction of the compression strut, which are the diagonal cracks in the concrete surface of specimens.

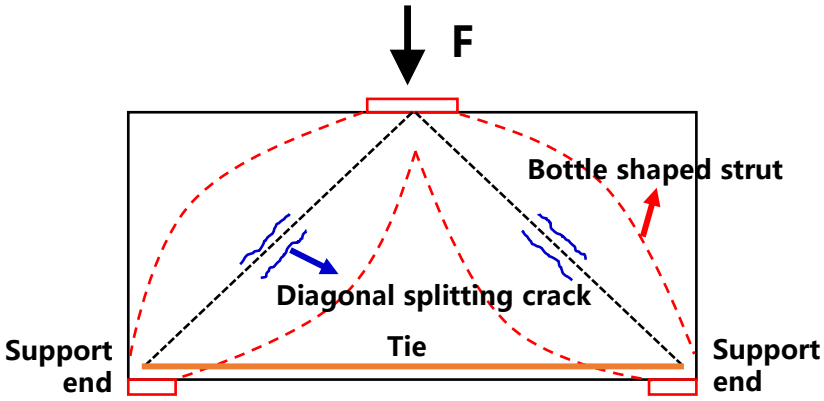


**Figure 11.** STM in simply supported deep beam.

### *3.2. Load–Displacement Response*

The load–displacement curves can be seen in Figure 12. The load values are determined from the test machine and the displacement values are the mean values of the two LVDT sensors. It can be seen that all the specimens exhibit the elastic and hardening deformation stage. During the elastic deformation stage, all the specimens show the similar load–displacement response and the end of the elastic deformation stage is referred to the yielding of the headed bars. In the hardening deformation stage until peak load, the load–displacement curves among all the specimens are also similar since the displacement value in the load–displacement curve is the sum of the tensile extension of the headed bar and the slip between the steel bar and concrete. The value of the slip is much smaller compared to the steel bar tensile extension after yielding, and therefore, the load–displacement curves basically represent the deformation of the headed bar under tension. Additionally, the ductility is various among the specimens with the same design parameters and it is due to the uneven bar stress and rotation of the specimens mentioned above. Additionally, the peak loads vary among different specimens even with the same design parameters, and come along with the stress differences among the headed bars. Since the headed bars are already in the strain-hardening deformation stage during the hardening stage of the specimens, small differences in the rebar stresses are accompanied by large differences in the rebar deformation. So, the ductility of specimens varies.

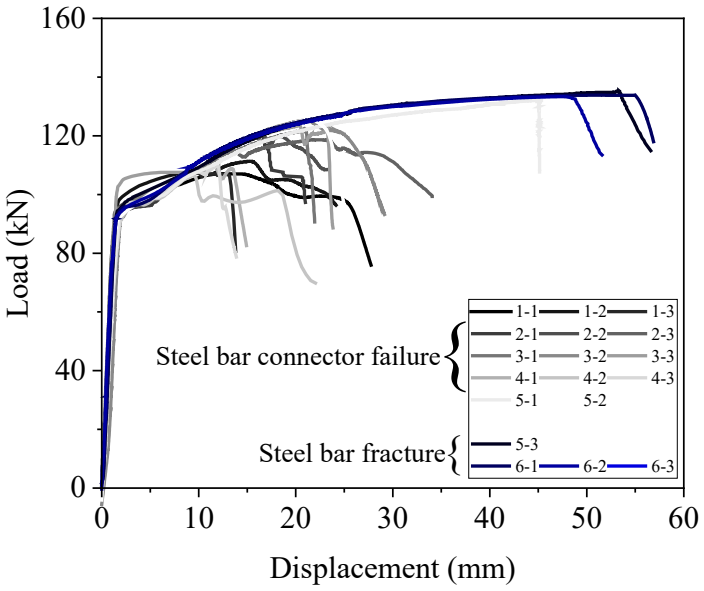


**Figure 12.** Load–displacement curves.

The bearing capacity of CHBC is the maximum load ($F_u$) applied to the headed bar during loading and its value is equal to the half of the peak load determined from the universal testing machine in this paper. Table 4 summarizes the values of the bearing capacity for CHBC. It can be seen that the bearing capacities for all the specimens are between the yield strength and ultimate tensile strength of the headed bar determined from the materials' tests. It should be noted that the bearing capacities of specimens with steel rupture failure are smaller than the rebar ultimate tensile strength. That is because half of the peak load determined from the universal testing machine is smaller than the load applied on the headed bar which is eventually ruptured. The uneven headed-bar stress of the specimens mentioned above should be responsible for such a situation.

**Table 4.** Experimental data of bearing capacity.

| No. | Specimen ID | $F_u$ (kN) | Average of $F_u$ (kN) | $F_{y,s}$ (kN) | $F_{u,s}$ (kN) | Failure Mode |
|---|---|---|---|---|---|---|
| 1 | M4-D12-6d | 53.6 | 54.6 | 50.7 | 69.8 | Steel bar connector failure |
| 2 | | 53.9 | | | | |
| 3 | | 56.2 | | | | |
| 4 | M4-D12-7.5d | 59.5 | 60.0 | 50.7 | 69.8 | Steel bar connector failure |
| 5 | | 60.0 | | | | |
| 6 | | 60.6 | | | | |
| 7 | M4-D12-9d | 61.1 | 62.0 | 50.7 | 69.8 | Steel bar connector failure |
| 8 | | 61.9 | | | | |
| 9 | | 63.1 | | | | |
| 10 | M3-D12-7.5d | 53.3 | 54.6 | 50.7 | 69.8 | Steel bar connector failure |
| 11 | | 55.2 | | | | |
| 12 | | 55.3 | | | | |
| 13 | M6-D12-7.5d | 63.4 | 65.8 | 50.7 | 69.8 | Steel bar connector failure |
| 14 | | 66.4 | | | | Steel bar connector failure |
| 15 | | 67.5 | | | | Steel bar rupture failure |
| 16 | M8-D12-7.5d | 66.4 | 66.7 | 50.7 | 69.8 | Steel bar rupture failure |
| 17 | | 66.7 | | | | |
| 18 | | 67.0 | | | | |

Note: $F_{y,s}$ and $F_{u,s}$ are the yield and ultimate tensile strength of the headed bar in the material test.

### *3.3. Effects of Main Variables on Bearing Capacity*

#### 3.3.1. Lap Length

As shown in Figure 13, with the increase in lap length, the bearing capacity of CHBC is improved. It is known that bond behavior together with the concrete compression at the head contributes to the bearing capacity. The bond capacity shows a positive correlation of the increase in lap length, so the increase in lap length improves the bearing capacity of CHBC.

The range of the bearing capacity of the specimens with a lap length varying from six to nine times the steel bar diameter is between the yield and ultimate tensile strength of the headed bar. Referring to Chinese design specification GB 50010-2020 [37], the required lap length is equal to about 32 times the steel bar diameter for straight rebar under the specimen design parameters in this paper. However, through the additional heads, a lap length of six times the steel bar diameter can guarantee the yielding of the steel bar. Lap length is saved in large quantities which is economically beneficial in construction since it can significantly reduce the length of reinforcement connection area and the on-site construction work is hence reduced.

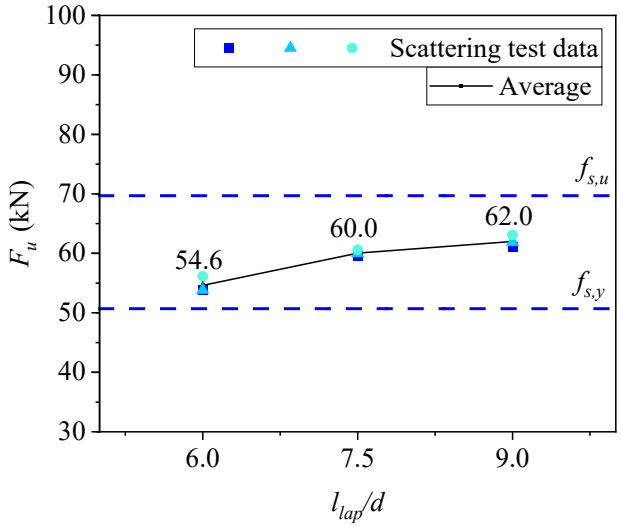


**Figure 13.** Relationship between lap length and bearing capacity.

3.3.2. Head Size

As shown in Figure 14, when the value of $A_h/A_s$ is equal to 3 to 6, the increase in head size improves the bearing capacity of the CHBC. The bigger heads bring the larger compression area of the diagonal strut between the heads, which improves the bearing capacity of the concrete strut as well as CHBC.

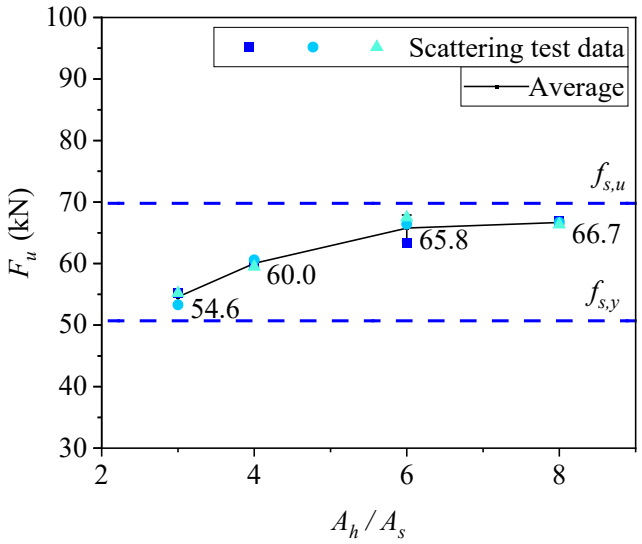


**Figure 14.** Relationship between head size and bearing capacity.

When the value of $A_h/A_s$ is larger than six, the improvement in the bearing capacity is less obvious with the increase in head size. The bearing capacity of the CHBC is actually the minimum of the headed-bar tensile strength and steel-bar connector-bearing capacity. Thus, the critical size of the head can be determined and the bearing capacity of CHBC with critical head size is just equal to the headed-bar tensile strength. Increasing the head size over the critical value cannot improve the bearing capacity of CHBC and those specimens with a head size equal or larger than the critical value should fail by the steel bar rupture. It should be noted that one of the three specimens of $A_h/A_s$ equal to six is failed by the steel bar rupture and all the three specimens of $A_h/A_s$ equal to eight are of steel-bar rupture failure mode. Then, the critical value of the head size should be varied from six to eight times the cross-sectional area of the headed bar when the lap length is equal to 7.5 times of the headed bar diameter.

To achieve the steel bar tensile strength, the lap length of CHBC with a head of critical size is only equal to about 0.24 times that of the straight bar slice specified in Chinese design specification GB 50010-2020 [37], a 76% reduction in lap length is achieved. In addition, by the confined stirrup, the lapping length of CHBC is about 0.36 times of the anchorage length of headed bar specified in Chinese design specification GB 50010-2020 [37], 64% reduction is achieved. It should be noted than the minimum $A_h/A_s$ is equal to five in the determination of anchorage length according to the code. The superiority of CHBC in saving the lap length for the steel bar splice is proved. Moreover, the minimum connection length for grouted sleeve splice is eight times of the rebar diameter with the compression strength of grouting materials being higher than 85 MPa according to Chinese specifications JGJ 355-2015 [49]. When compared to the grouted sleeve splice connection, although the lap length in CHBC is not decreased, the requirements for grouting and high-strength grouting materials are eliminated, which can help save in construction costs and time.

### *3.4. Strain Development of Stirrup*

Strain development of stirrups for all the specimens is similar. Take specimen M4-D12-7.5d as an example (Figure 15). The stirrups can be divided into two types in this study, the confined stirrup and the general stirrup (Figure 5b). The confined stirrup locates at the lap length zone between the heads and across the diagonal cracks. For the confined stirrups, the strains develop slow before the peak load of the specimens. At peak load, the diagonal cracks are developed at the concrete surface and the strains of confined stirrups develop fast, which can restrain the expansion of cracks. At the post-peak load stage, the strains of the confined stirrup develop rapidly. In terms of general stirrups, although the strains of general stirrups develop rapidly in the post-peak load stage, the strain values of the general stirrups are still smaller than 1000 $\mu\varepsilon$, far below the yielding strain, during the whole loading process. Since the adjacent headed bars are not coaxial and it can result in the rotation of CHBC, the general stirrups are adopted to simulate the constraint of the other reinforcements in structure members on CHBC. The strain values of the general stirrup being small indicates that while CHBC is applied in the concrete structure, adequate constraint can be guaranteed to limit the adverse effects caused by the rotation of CHBC.

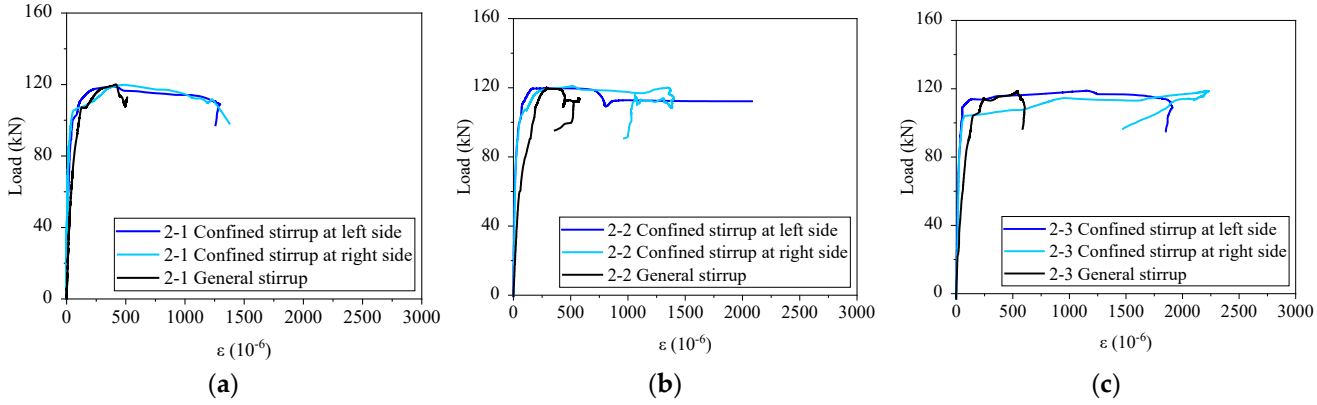


**Figure 15.** Strain development of stirrup (**a**) M4-D12-7.5d-1; (**b**) M4-D12-7.5d-2; (**c**) M4-D12-7.5d-3.

The confined stirrup can strengthen the core concrete, which can improve the bearing capacity of CHBC. In addition, the confined stirrups are across the diagonal crack region. Then, the confined stirrup may be under shear deformation due to dowel action, which can contribute to the bearing capacity of CHBC directly by the projection of shear force in the axial direction of headed bar. The removal of concrete after the test has been conducted shows that the confined stirrup skeleton is integrated and little shear deformation is observed (Figure 16). Therefore, the confined stirrup mainly sustains tension force and functions to provide confinement to the core concrete instead of bearing the shear force.

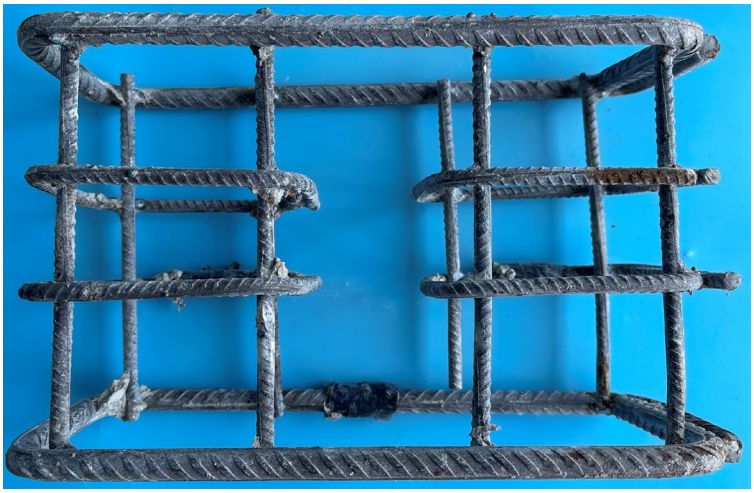

**Figure 16.** Stirrup skeleton after the test.

To achieve a good confinement to the core concrete, the spacing between the confined stirrups should not be too large within the lap length. It is recommended in this paper that the spacing of the confined stirrups should meet the requirement that at least two confined stirrups should be placed between the heads in order to provide a good confinement. Additionally, the diameter of the confined stirrup rebar is recommended to be greater than 6 mm.

### *3.5. Distributive Relationship of Headed Bar Force*

It is known that the collaboration of bond behavior force and concrete compression-bearing force at the head resists the load of CHBC under tension. Strain gauges are arranged at the headed bars by the side of head-bearing surface and then, the concrete compression-bearing force at the head can be obtained through the simple calculation $F_h = E_s\ \varepsilon_h\ A_s$, where $\varepsilon_h$ is the strain gauge data. While the headed rebar is subjected to tensile load ($F_s$ denotes the tensile load), the force carried by bond behavior, $F_b$, is the difference between $F_s$ and $F_h$. It should be noted that there are four gauging points within one single specimen and the average values of a total of twelve gauging points for three specimens of same design parameters are adopted in the following discussion.

#### 3.5.1. Effects of Lap Length

The distributive relationship between bond behavior and head bearing among specimens with different lap lengths is given in Figure 17. The plateau region of the curves represents the yielding of headed bars. It can be concluded that the increase in lap length reduces the contribution by head bearing with the increased contribution by bond behavior. Details can be seen in the following.

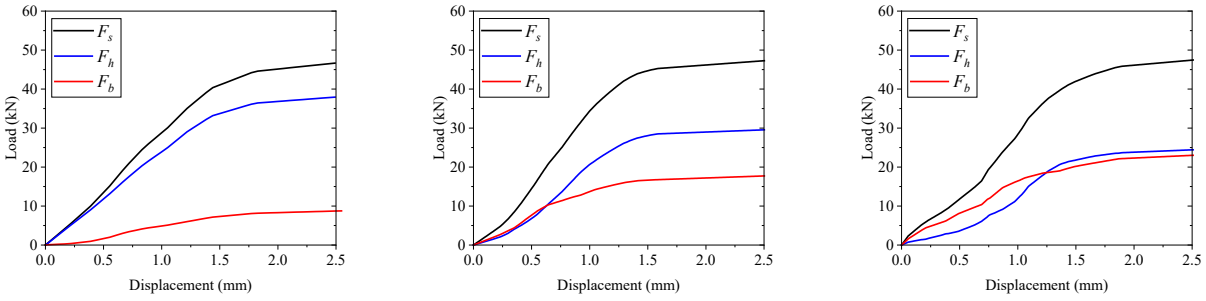


**Figure 17.** Distribution of headed bar force among specimens with different lap length (**a**) Specimen M4-D12-6d; (**b**) Specimen M4-D12-7.5d; (**c**) Specimen M4-D12-9d.

At the early stage of loading, for the specimens with a smaller lap length (specimen M4-D12-6d), the headed bar tensile force is mainly carried by concrete compression at the head; for the specimens with a lap length equal to 7.5 times the headed bar diameter (specimen M4-D12-7.5d), these two force components are close to each other; for the specimens with a larger lap length (specimen M4-D12-9d), the force carried by the concrete compression at the head is smaller than that sustained by the bond behavior. In terms of stiffness, the stiffness of CHBC is the superposition of the concrete compression stiffness at the head and the stiffness of the bond behavior. At the early stage of loading, for the specimens with a smaller lap length (specimen M4-D12-6d), the stiffness of the head bearing is significantly larger than that of the bond; for the specimens with a lap length equal to 7.5 times the headed bar diameter (specimen M4-D12-7.5d), these two stiffness components are close to each other but with increase in the tensile load, the stiffness of the head bearing tends to be greater than that of the bond; for the specimens with a larger lap length (specimen M4-D12-9d), the stiffness of the head bearing is lower than that of the bond but similar to specimen M4-D12-7.5d, the stiffness of the head bearing tends to be greater than that of the bond as the load increases. The $F_b/F_h$ values for the yielding of headed bars are given in Figure 18. Approximately, the $F_b/F_h$ values increase linearly with the lap length, and the larger value of $F_b/F_h$ indicates the lower contribution of the head bearing with more contributed by bond behavior. When the lap length of six times the headed bar diameter is increased by 25% and 50%, the $F_b/F_h$ value is increased by 160.9% and 310.0%, respectively. In summary, in terms of the load-bearing contribution and stiffness, the increase in lap length decreases the contribution by head bearing.

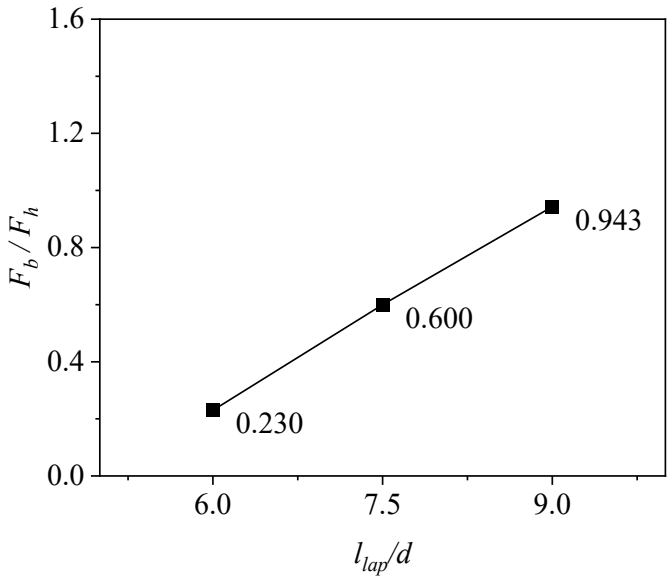


**Figure 18.** Relationship between $F_b/F_h$ and lap length.

In the comparison of head bearing among specimens with a different lap length, similarity in stiffness of head bearing can be found as highlighted in Figure 19. The reason for the trend is that the head bearing functions as the concrete at the head is under compression, then the stiffness of the head bearing is actually related to the concrete compression elastic modulus. Since the same concrete and head geometry are adopted among these three types of specimens, similarity is thus found for their stiffness of head bearing.

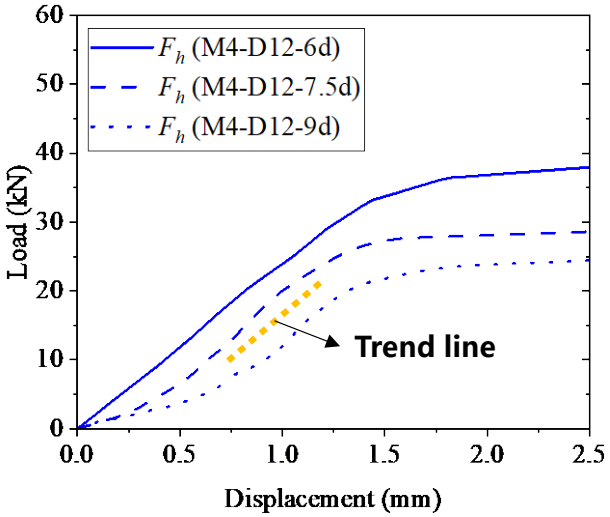


**Figure 19.** Comparison of head bearing among specimens with different lap length.

The bond force and average bond stress before the yielding of the headed bar are shown in Figure 20. The average bond stress is determined by $\overline{\tau} = F_b/(\pi d l_{lap})$. When the lap length of six times of the headed bar diameter is increased by 25% and 50%, the value of $F_b$ is increased by 103.0% and 163.8%, respectively, while the average bond stress is increased by 62.1% and 71.9%, respectively. Additionally, the development of average bond stress for specimen M4-D12-7.5d and specimen M4-D12-9d is similar. In addition, for specimens with a different lap length, the average bond stress is approximately linearly increased with the applied tension load.

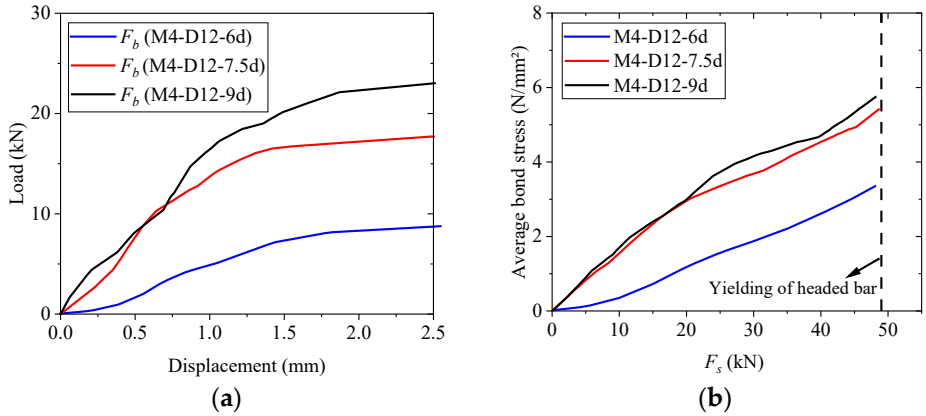


**Figure 20.** Bond behavior with different lap length (**a**) Bond force; (**b**) Average bond stress.

### 3.5.2. Effects of Head Size

The distributive relationship of bond behavior and head bearing among specimens with different head sizes is shown in Figure 21. Additionally, the plateau region of the curves represents the yielding of headed bars. For the head size increases from $3A_s$ (specimen M3-D12-7.5d) to $4A_s$ (specimen M4-D12-7.5d), both the head-bearing stiffness at an early stage and the head-bearing force at the yielding of headed bars increase. For the head size increases from $4A_s$ (specimen M4-D12-7.5d) to $6A_s$ (specimen M6-D12-7.5d), a slight decrease can be observed in the stiffness of the head bearing at an early stage with a small increase in the head-bearing force at the yielding of the headed bars. For the head size increases from $6A_s$ (specimen M6-D12-7.5d) to $8A_s$ (specimen M8-D12-7.5d), both the stiffness and head-bearing force change little.

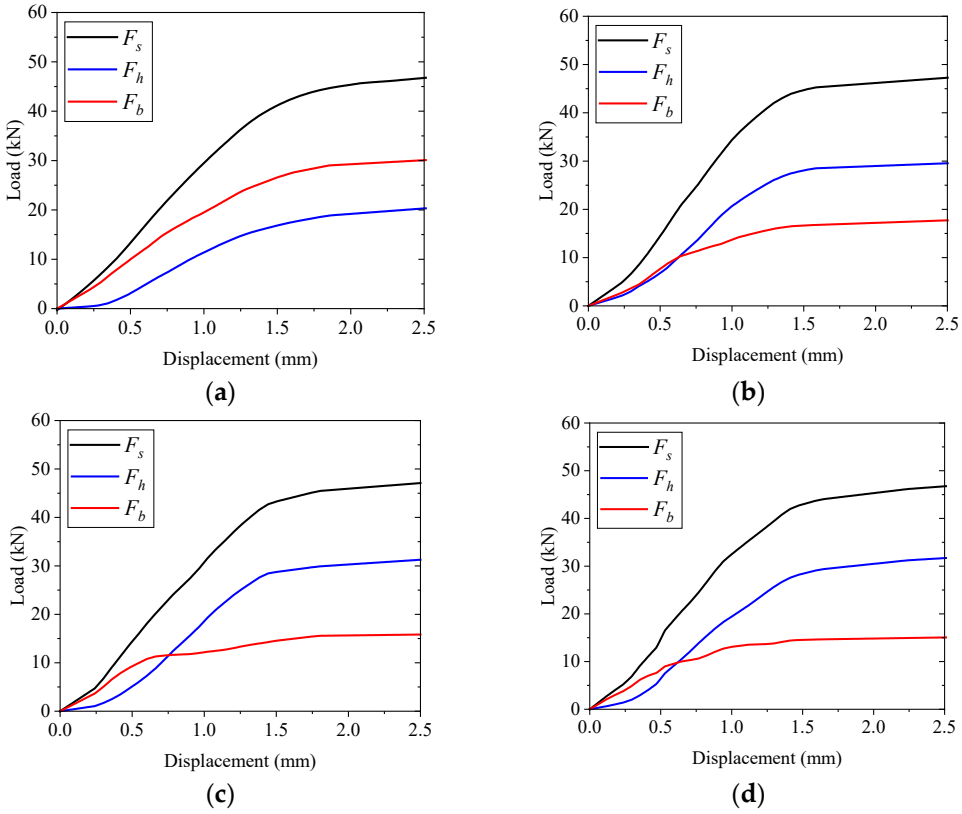


**Figure 21.** Distribution of headed bar force among specimens with different head size (**a**) Specimen M3-D12-7.5d; (**b**) Specimen M4-D12-7.5d; (**c**) Specimen M6-D12-7.5d; (**d**) Specimen M8-D12-7.5d.

The $F_b/F_h$ values for the yielding of headed bars are shown in Figure 22. In general, the $F_b/F_h$ values decrease with the increase in the head size, indicating the increase in head size improves the contribution by head bearing. In general, the head-bearing force and the stiffness improve with the increase in head size. Additionally, when the head size is increased by 100% (increasing from $4A_s$ to $8A_s$), the $F_b/F_h$ value is decreased by 20.8% and the change in the $F_b/F_h$ value induced by the change of head size is considerably smaller than that of the lap length. In addition, specimen M3-D12-7.5d shows a remarkable difference compared to other specimens. Similar situations can be seen in Figure 23 in which both the head-bearing response and bond behavior of specimen M3-D12-7.5d are distinct from the other specimens which show a similar response.

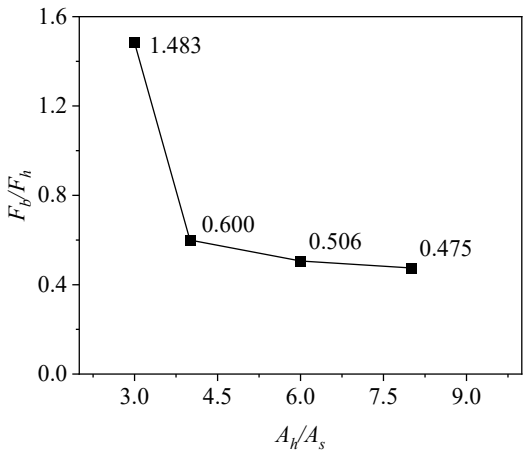


**Figure 22.** Relationship between $F_b/F_h$ and head size.

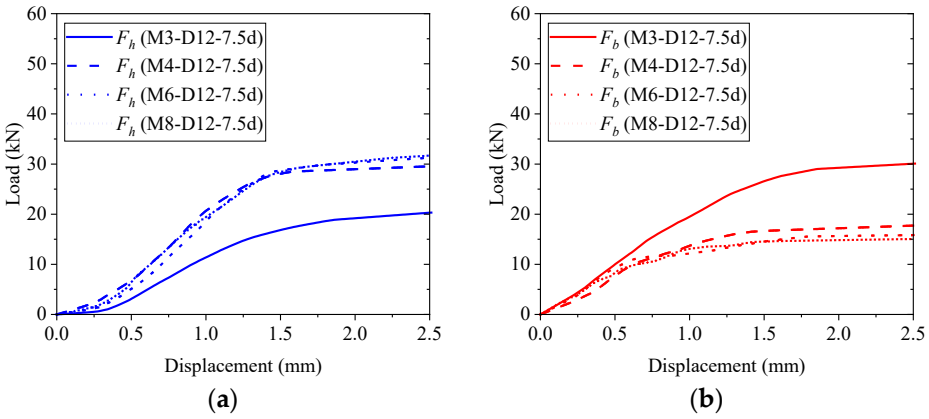


**Figure 23.** Comparison of head bearing and bond among specimens with different head size (**a**) Head bearing; (**b**) Bond behavior.

Although the change in head size can induce the change in head-bearing response, the reasons for the enormous difference for specimen M3-D12-7.5d may be caused by the specimen's manufacture. Perforated plug welding (Figure 24) is adopted in the connection of head and headed bar, while welding fillet on the head-bearing surface is inevitable. Such a welding fillet effect can reduce the bearing surface area of the head and therefore, the head-bearing capacity is diminished. For specimen M3-D12-7.5d, the difference between the head and steel bar in dimension is relatively small. The side length of the square head is equal to 18 mm while the diameter of the headed bar is equal to 12 mm for specimen M3-D12-7.5d. So, the welding fillet effect is strong and it can greatly reduce the bearing surface area of the head, which changes the contribution by head bearing to a great extent.

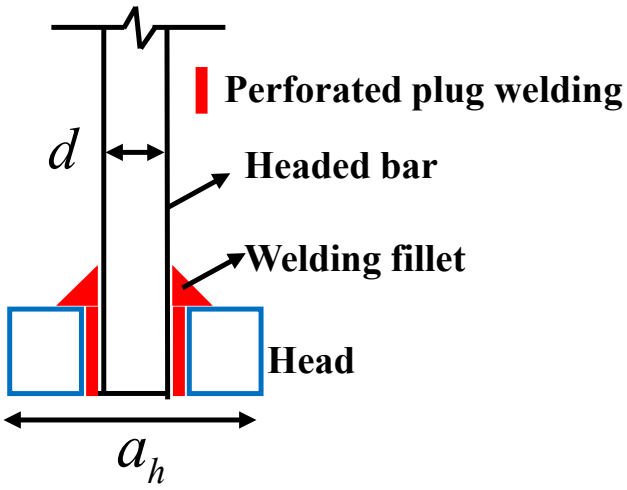


**Figure 24.** Connection between head and steel bar.

The average bond stress before yielding of headed bar is shown in Figure 25. When the head size is increased by 100% (increasing from $4A_s$ to $8A_s$), the value of $F_b$ is decreased by 15.0% and the average bond stress is decreased by 16.8%. In addition, the average bond stress and bond stiffness of specimen M3-D12-7.5d is significantly higher than the other specimens which show a similar bond stress development, due to the welding fillet effect mentioned above. Additionally, the average bond stress of specimen M3-D12-7.5d is larger than the peak bond stress specified in Chinese code GB/T 50010-2020 [37] which is equal to three times the concrete tensile strength. It should be noted that the peak bond stress is related to the concrete cover thickness and stirrup ratio and the required concrete cover thickness specified in Chinese code GB/T 50010-2020 [37] is two times larger than the steel bar diameter. For all specimens, the concrete cover thickness of the headed bar satisfies the code's requirements. In addition, the confined stirrup in CHBC can improve the bond

strength. Then, it can be inferred that at the ultimate bearing capacity of CHBC, the average bond stress is larger than the peak bond stress in code.

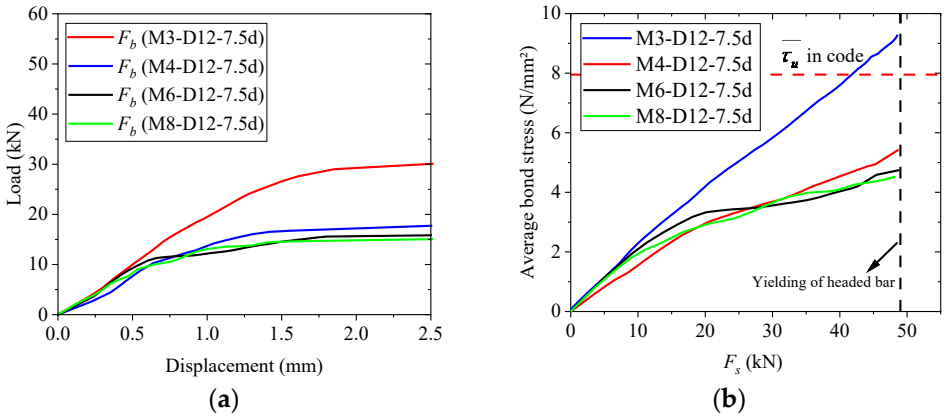


**Figure 25.** Bond behavior with different head size (**a**) Bond force; (**b**) Average bond stress.

### *3.6. Slip Behavior*

Micrometer calipers are adopted to measure the slip values at the loading end and free end (Figure 5a). The slip value at the free end is equal to the value of concrete compression deformation by head bearing. The slip value at the load end contains the concrete compression deformation and slip between the headed bar and concrete as well as the tensile deformation of headed bar. So, the value of slip between the headed bar and concrete can be determined from the measured slip value at the load end subtracted by the superposition of measured slip value at the free end and the headed-bar tensile deformation. Similarly, the average values of a total of twelve measurement points for three specimens of the same design parameters are adopted in the following discussion.

#### 3.6.1. Load–Slip Response

The load–slip curves of all specimens are plotted in Figure 26 before the headed bars are yielded and 'BS' in the figure stands for bond slip while 'HB' denotes the concrete compression deformation by head bearing. In general, it can be seen that the slips due to bond behavior are larger than the concrete compression deformations by head bearing for all the specimens.

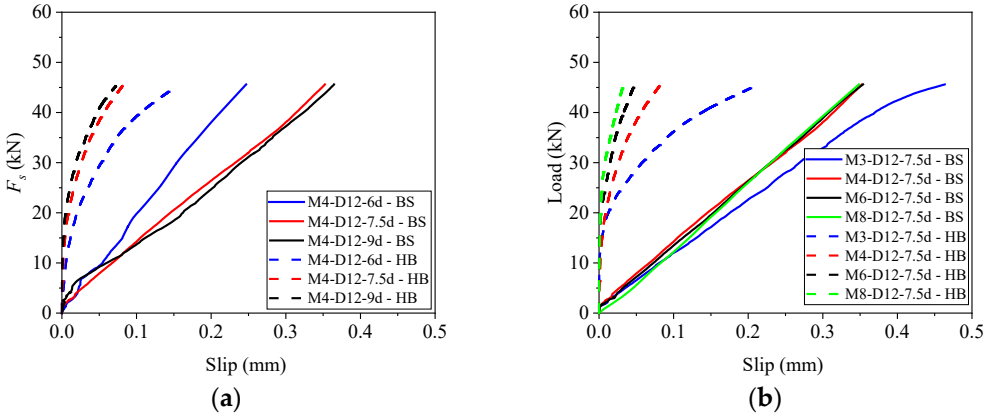


**Figure 26.** Load–slip curves (**a**) Comparison of different lap length; (**b**) Comparison of different head size.

For specimens with a different lap length and the same head size (Figure 26a), specimen M4-D12-6d with the minimum lap length shows the minimum bond slip with maximum head compression deformation while the other specimens show a similar load–slip response.

When the headed bar is yielding, the lap length of six times the headed bar diameter is increased by 25% and 50%, and the bond slip is increased by 43.1% and 48.4%, respectively.

For specimens with the same lap length and a different head size (Figure 26b), specimen M3-D12-7.5d with the minimum head size shows the maximum bond slip and head compression deformation. When the headed bar is yielding, the bond slip of specimen M3-D12-7.5d is 31.5% larger than that of specimen M4-D12-7.5d. In addition, the values of concrete compression deformation decrease with the increase in head size.

#### 3.6.2. Interaction with the Force Distribution Relationship

The average bond stress–slip curve before the yielding of the headed bar is shown in Figure 27. In general, before yielding, the bond stress is approximately linearly increased with the slip which indicates that the bond–slip relationship is in the elastic range before yielding. In addition, the bond stiffness is smaller than that of the straight bar without head specified in Chinese code GB 50010-2020 [37]. Concrete is under compression due to head bearing and the slip is the deformation difference between steel bar and concrete. So, the slip becomes larger because of the additional concrete compression deformation of head bearing for the headed bar when compared to the straight bar without a head and the larger slip indicates the smaller bond stiffness.

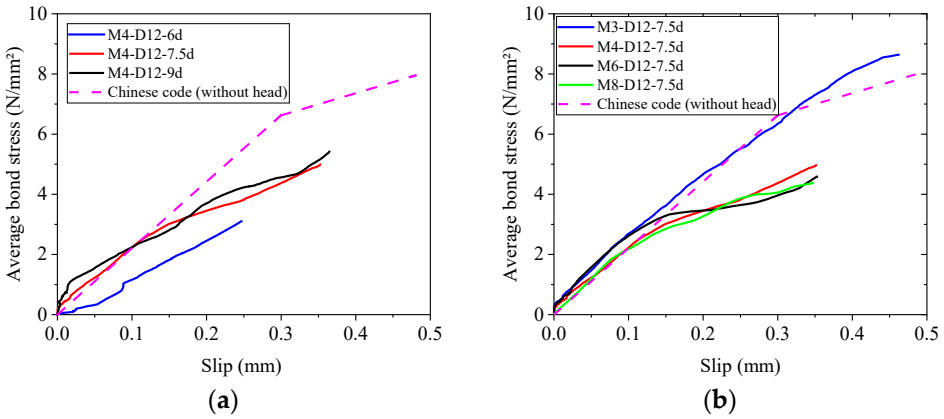


**Figure 27.** Average bond stress–slip curve (**a**) Comparison of different lap length; (**b**) Comparison of different head size.

For specimen M4-D12-6d, the head bearing functions more while the bond behavior functions less when compared to other specimens (Figure 17) and the average bond stress of specimen M4-D12-6d is smaller than that of other specimens as shown in Figure 27a. Based on the relationship between slip and force, it indicates a larger concrete compression deformation at heads and a smaller bond slip for specimen M4-D12-6d when compared to other specimens. Such a tendency is consistent with the trend in Figure 26a.

For specimen M3-D12-7.5d, the head bearing functions less while the bond behavior functions more when compared to other specimens (Figure 21) and the average bond stress is higher than other specimens as shown in Figure 27b, indicating a larger bond slip as shown in Figure 26b. However, for specimen M3-D12-7.5d, the head-bearing force is smaller (Figure 22) while the concrete compression deformation at the head is even larger when compared with other specimens as shown in Figure 26b. The head size of specimen M3-D12-7.5d is the smallest one and moreover, due to the welding fillet effect, the bearing surface area of specimen M3-D12-7.5d is reduced significantly. It is known that the concrete stress is inversely proportional to the bearing area under the same compression force and therefore, then the concrete compression strain or deformation is also inversely proportional to the bearing area. So, even with the smallest head compression force, specimen M3-D12-7.5d with the smallest head size and head-bearing surface area shows the largest head-compression deformation. In addition, head sizes are increased incrementally across specimen M4-D12-7.5d, specimen M6-D12-7.5d and specimen M8-

D12-7.5d while these three types of specimens show a similar head-bearing force. So, the concrete compression deformation at the heads should show the decreased tendency across these three specimens, which is consistent with the trend in Figure 26b.

#### 3.6.3. Interrelationship of Lap Length and Head Size

Specimen M4-D12-6d and specimen M3-D12-7.5d show a similar bearing capacity. Comparisons are made between these two specimens in Figure 28. Bond behavior functions less and head-bearing functions more for specimen M4-D12-6d with the smaller lap length and larger head size when compared to specimen M3-D12-7.5d. When the headed bar is yielding, the $F_b$ value of specimen M3-D12-7.5d is 245.2% larger than that of specimen M4-D12-6d while the average bond stress is 158.2% larger. Moreover, the bond slip of specimen M3-D12-7.5d is 88.2% larger than that of specimen M4-D12-6d. As illustrated above, the bond slip is related to the distributive proportion of bond behavior and average bond stress. The larger lap length indicates the larger distributive proportion of bond behavior as well as larger bond stress, which results in the larger bond slip values. It should be noted that the increase in bond slip is harmful to the stiffness of CHBC.

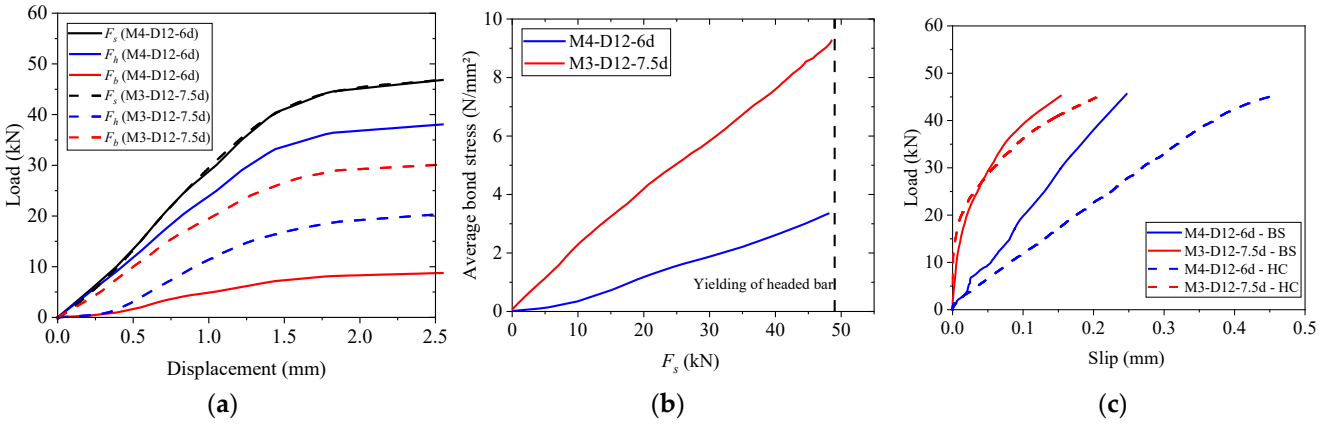


**Figure 28.** Comparison between specimen M4-D12-6d and M3-D12-7.5d (**a**) Distributive relationship; (**b**) Average bond stress; (**c**) Load–slip curve.

To achieve the adequate bearing capacity of CHBC, a guarantee should be made on the adequate lap length and head size. However, it is worth increasing the head size in order to improve the bearing capacity of CHBC, because the use of a larger head size can render the use of the smaller lap length with less bond behavior as well as bond slip. So, it is recommended to use the large head if the congestion caused can be handled in construction.

## 4. Numerical Investigation

The finite element method has been adopted to study the mechanism of CHBC using ABAQUS.

### *4.1. Finite Element Modeling*

In order to reduce the computing time, half of the specimen has been modelled based on the specimen symmetry (Figure 29).

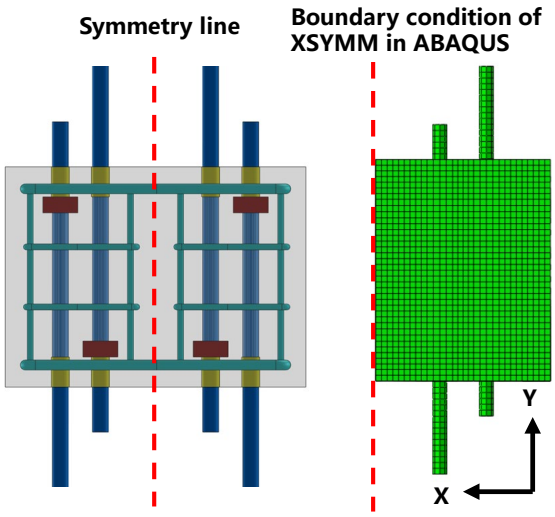


**Figure 29.** Modeling in ABAQUS.

The element type of C3D8R is adopted for the head, headed bar and concrete object and T3D2 element type is adopted to mesh the stirrup object. The CDP model is used to simulate the plastic behavior of concrete. In addition, the concrete material definition refers to Teng's [50] research work in order to consider the stirrup confinement effect. The elasto-plastic tri-linear model is adopted to define the steel materials including head and steel bar. The bond behavior between steel bar and concrete is simulated by the nonlinear connector in ABAQUS. Besides, the bond stress versus slip relationship is determined based on the Chinese specification GB 50010-2020 [37]. Verification of the finite element model in terms of load–displacement curves can be seen in Figure 30.

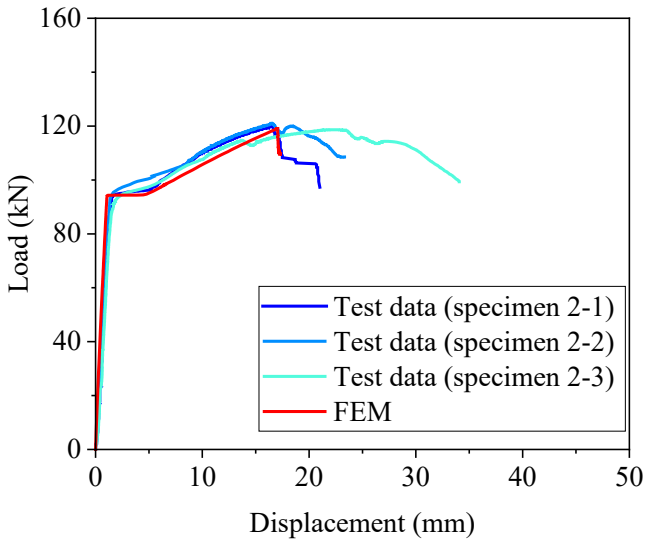


**Figure 30.** Verification of the finite element modeling.

*4.2. Crack Pattern*

The diagonal cracks between the heads are a very common phenomenon observed during the test among all the specimens. The predicted crack pattern in ABAQUS through tensile strain at concrete surface is shown and a comparison between the experimental observation and prediction has been made in Figure 31. It can be seen that the crack patterns are quite similar between the experimental and numerical results.

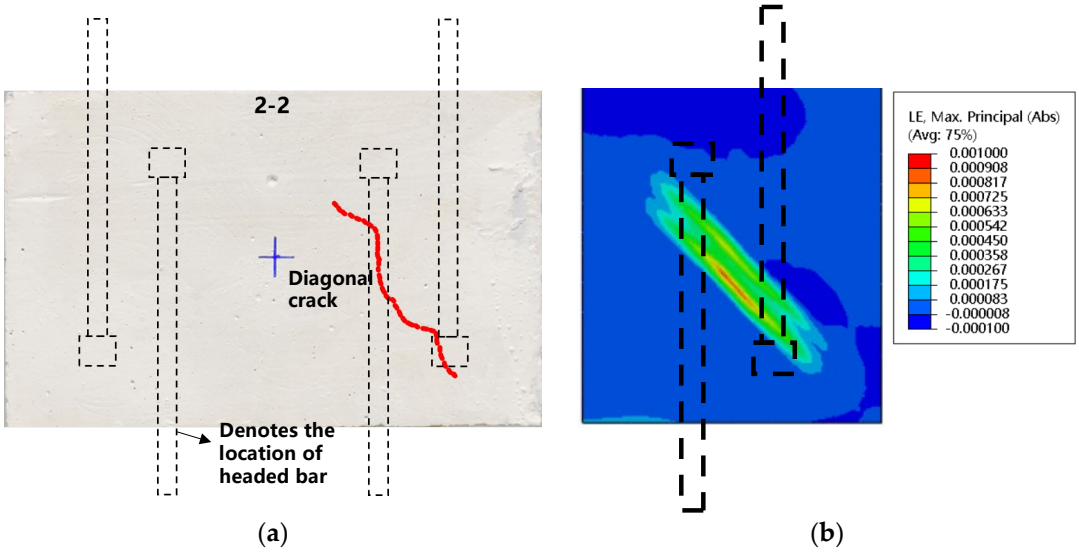


**Figure 31.** Crack pattern of experimental and numerical observation.

### *4.3. Concrete Compression at Head*

In order to study the concrete stress distribution at heads, sectioning of the specimen has been conducted and the concrete stress contour can be seen in Figure 32.

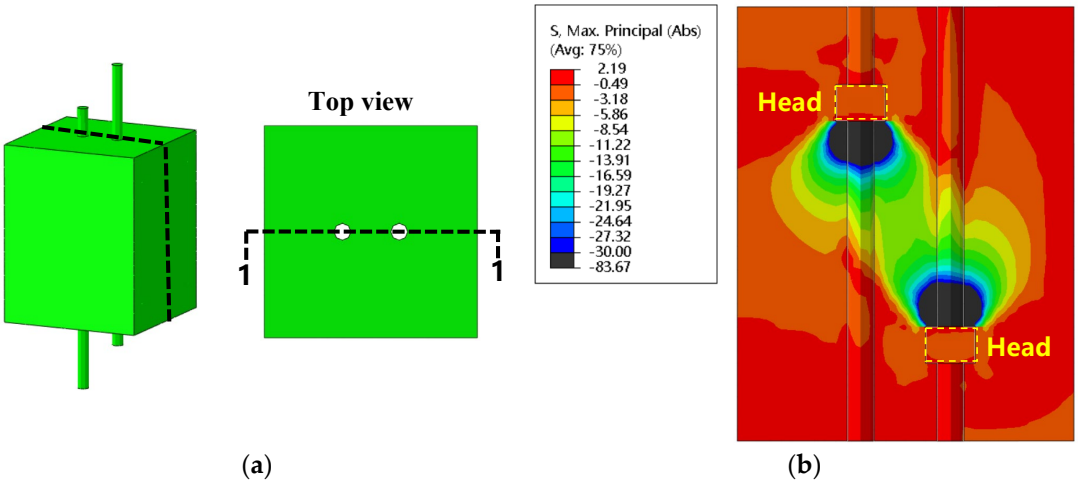


**Figure 32.** Concrete stress contour (**a**) Section of the specimen; (**b**) Maximum principal stress contour at 1-1 section.

It can be seen that high compressive stress can be observed in the nearby area of the heads. In addition, a compression stress zone is observed located at the region between the two heads, which generates the diagonal compressive strut. The diagonal compressive strut can be observed in Figure 33, which only displays the element in compressive stress situation with the elements in tensile-stress situation being hidden. The angle $a$ between the diagonal compression strut and headed bar is proposed and it can be calculated through the following Equation (1):

$$\tan a = s/l_{lap} \quad (1)$$

where $s$ is the spacing of the adjacent headed bar; $l_{lap}$ is the lap length.

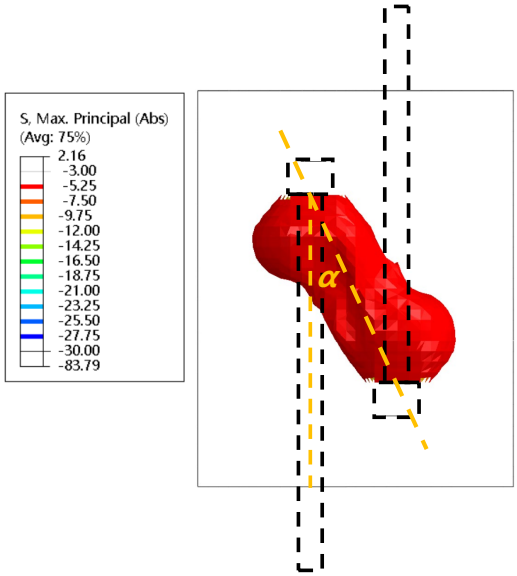


**Figure 33.** Diagonal compressive strut between two heads.

Comparisons are made and shown in Figure 34 between the diagonal cracks in tests and the proposed *a* angle. It can be seen that the direction of the *a* angle matches with the direction of diagonal cracks. It validates the accuracy of the proposed method to determine the diagonal strut angle *a*.

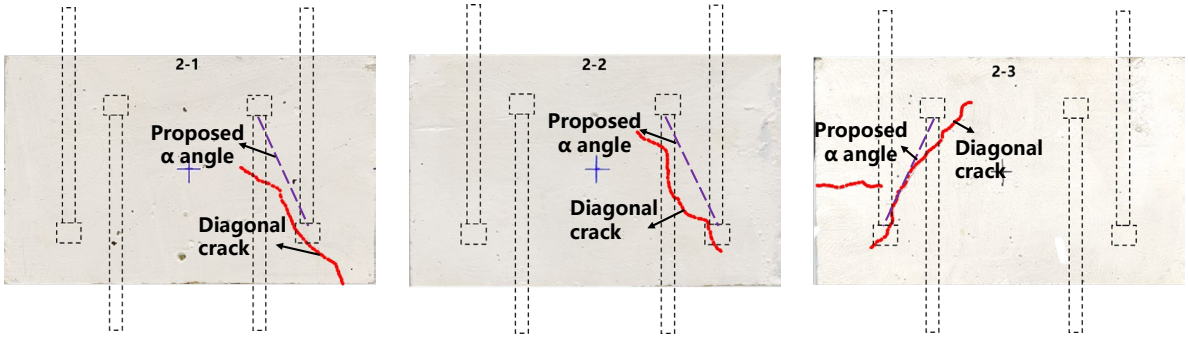


**Figure 34.** Angle *a* against the direction of diagonal crack of specimen M4-D12-7.5d.

Through the stress vector contours in Figure 35, the diagonal strut can be recognized of the bottle shape, which is the same as the strut in STM model. Again, the direction of the compressive stress vectors matches the angle *a*. For the diagonal strut, the compression-bearing area near the head is smaller but with a higher compression stress compared to that of the middle height between the two heads.

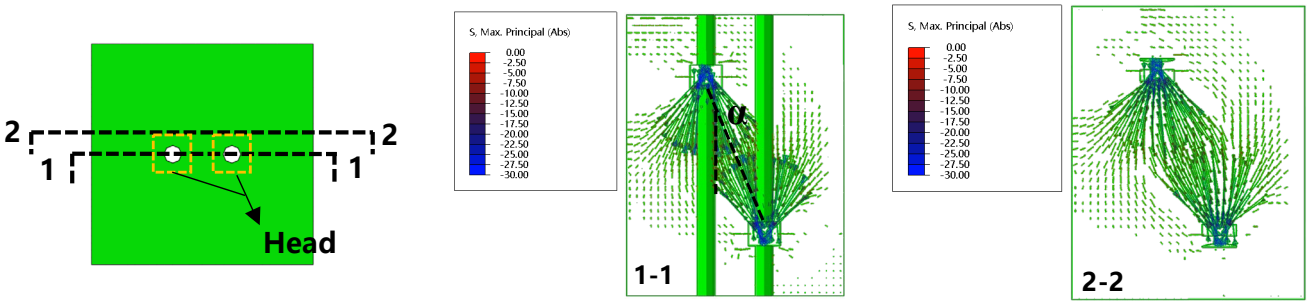


(**a**) (**b**) (**c**)

**Figure 35.** Compressive stress vector contours (**a**) Top view (**b**) 1-1 section (**c**) 2-2 section.

A similar stress distribution can be found in Figure 36. When the section locates at the head (section 1-1 and section 5-5), the high compression stresses can be observed nearby the head. As the section moves to the medium height of the lap length, the compression stresses decrease while the compression region area is increased. Such a trend is consistent with the stress distribution in the diagonal strut of the bottle shape.

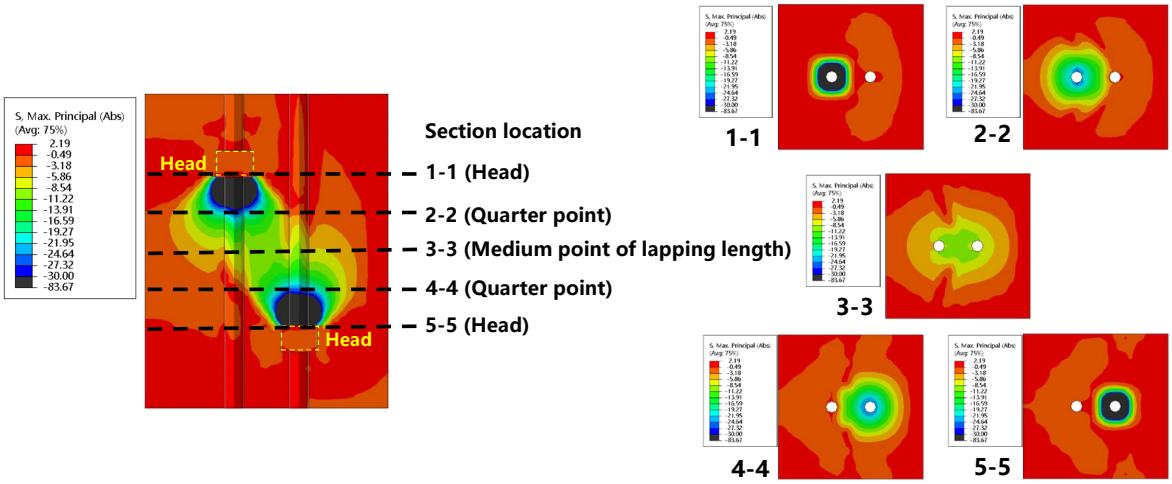


**Figure 36.** Stress contour at different level of height.

## 5. Design Method

### *5.1. Bearing Capacity Contributed by Bond and Head*

The basic form of the CHBC is steel bar splice which can be treated as the mutual anchorage of two steel bars. So, the bearing capacity of CHBC can be regarded as the anchorage capacity of single headed bar. In addition, it is known that the bearing capacity of CHBC consists of the bond behavior force and concrete compression-bearing force at head (Figure 37). Therefore, based on the superposition method, Equation (2) can be obtained:

$$F_u = F_{h,u} + F_{b,u} \tag{2}$$

where $F_u$ is the bearing capacity of the CHBC; $F_{h,u}$ is the contribution by concrete compression at head; $F_{b,u}$ is the contribution by bond behavior.

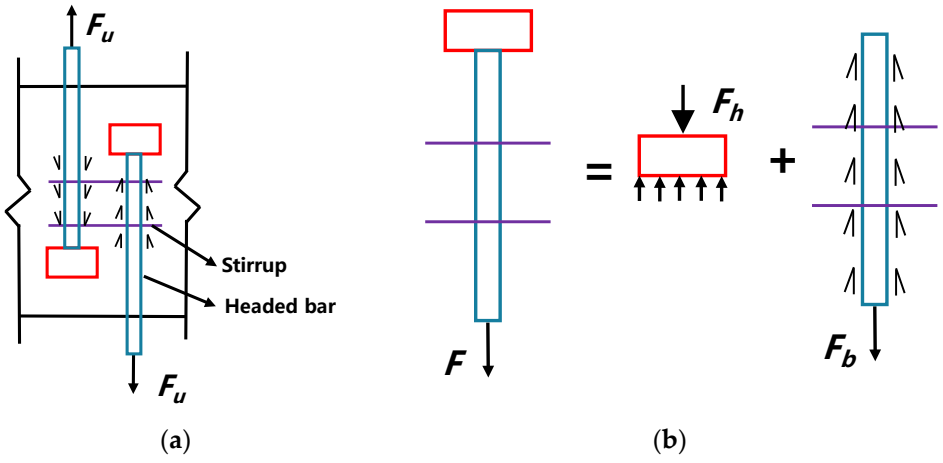


**Figure 37.** Capacity of CHBC (**a**) Sketch of the CHBC; (**b**) Head bearing and bond behavior.

To determine the $F_{h,u}$, the STM model as shown in Figure 38 is adopted.

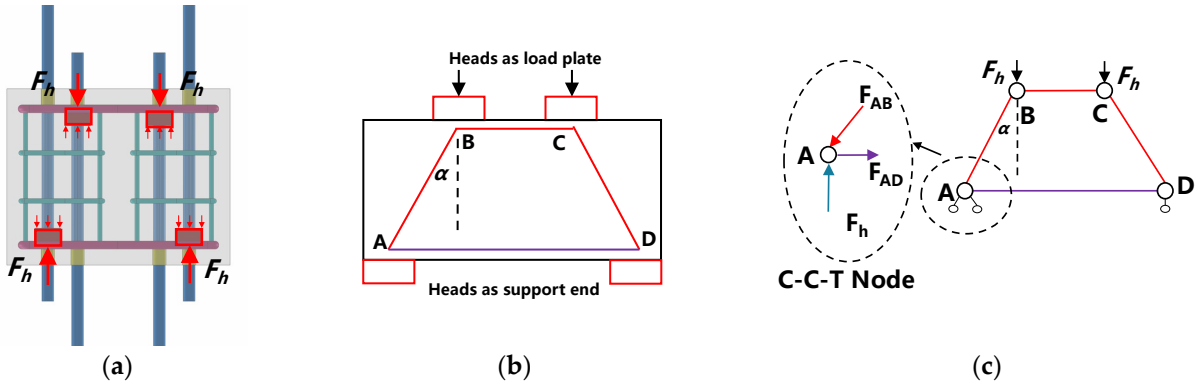


(**a**) (**b**) (**c**)

**Figure 38.** Strut-and-tie model (**a**) Force at heads; (**b**) STM model; (**c**) C-C-T node.

Under the tension of headed bars, the heads are under compression. The heads are assumed to be a rigid body, then the heads can be considered as the load plate and support end in the beam. So, it can be regarded as the concrete beam with a small shear-span ratio subjected to shear force. Then, the force transmission mechanism at the lap zone concrete can be described as the trapezoidal truss. The *AB* component together with the *CD* component in the STM model is the diagonal concrete strut and the angle of the strut is the angle *a* mentioned above while the *AD* component represents the tension tie of stirrup. The forces are balanced at node *A* or node *D* and it can be regarded as the C-C-T node. Then, based on the trigonometric relation, the following Equation (3) can be determined:

$$\begin{aligned} F_{AB} &= F_h / \cos\alpha \\ F_{AD} &= F_h \tan\alpha \end{aligned} \tag{3}$$

The capacity of the diagonal strut (*AB* component) is the multiplication of the strut cross-sectional area and concrete strength. The depth of the strut is equal to the side length of the square head [41] while the width of the strut can be determined according to Collins' and Michell's studies [51]. In addition, the concrete in CHBC is confined by the stirrup and therefore, the confined concrete strength should be adopted instead. The definition of the confined concrete strength is provided by the research work of Mander [52]. It should be noted that the unconfined concrete strength is equal to the cubic concrete strength in the material test of this paper in order to verify the prediction accuracy while the design concrete strength can be adopted in design for safety. In addition, the yield strength of the stirrup is adopted to determine the capacity of the tension tie (*AD* component). The capacity of the diagonal strut and tension tie can be determined through Equation (4):

$$\begin{aligned} F_{AB} &= f_{cc} a_h l_{lap} \sin a \\ f_{cc} &= f_c(-1.254 + 2.254\sqrt{1 + \tfrac{7.94 f_l'}{f_c}} - 2\tfrac{f_l'}{f_c}) \\ \tan a &= s / l_{lap} \\ F_{AD} &= n \times f_{y,v} \times A_{s,v} \end{aligned} \tag{4}$$

where $n$ is the number of the stirrup rebars; $f_{y,v}$ and $A_{sv}$ are the tensile strength and cross-sectional area of the stirrup rebar.

Capacity of the C-C-T node is limited by the strength of concrete compression strut and stirrup tension tie. So, Equation (5) can be adopted to determine the C-C-T node strength as well as the $F_{h,u}$:

$$F_{h,u} = \min\left\{ \begin{array}{l} F_{AB}\cos a \\ F_{AD} / \tan a \end{array} \right\} = \min\left\{ \begin{array}{l} f_{cc} a_h l_{lap} \sin a \cos a \\ n f_{y,v} A_{s,v} / \tan a \end{array} \right\} \tag{5}$$

It is known that the bond stress is unevenly distributed along the anchorage length for steel bar. The uneven distribution relationship can be described by Equation (6) referring to Xu's study [53]:

$$\tau(x)/\overline{\tau} = \begin{cases} 1.35\left[1-\left(1.25\frac{x}{l_a}-1\right)^2\right] & (0 < x \le 0.8l_a) \\ 1.35\sqrt{1-\left(5\frac{x}{l_a}-4\right)^2} & (0.8 < x \le l_a) \end{cases} \quad (6)$$

Based on the distributive relationship, the total forces integrated by bond stress can be determined by Equation (7):

$$\begin{aligned} F_\tau &= \pi d \int_0^{l_a} \tau(x)dx \\ &= \pi d\overline{\tau}\left(\int_0^{0.8l_a} 1.35\left[1-\left(1.25\frac{x}{l_a}-1\right)^2\right]dx + \int_{0.8l_a}^{l_a} 1.35\sqrt{1-\left(5\frac{x}{l_a}-4\right)^2}dx\right) \\ &= 0.932\pi d l_a \overline{\tau} \end{aligned} \quad (7)$$

As mentioned above, at the bearing capacity of CHBC, the average bond stress is larger than the peak bond stress specified in Chinese code GB 50010-2020 [37]. So, for conservative purposes, the load carried by the bond behavior in CHBC can be determined by Equation (8). It should be noted that the minimum concrete cover thickness for headed bar is equal to two times of the reinforcement diameter:

$$F_{b,u} = \pi d \int_0^{l_a} \tau(x)dx = 0.932\pi d l_a \overline{\tau_u} = 2.796 f_t \pi d l_{lap} \quad (8)$$

where $\overline{\tau_u}$ is the peak bond stress in code; $f_t$ is the tensile strength of concrete and it is equal to $0.395 {f_{cu}}^{0.55}$ in this paper.

In conclusion, the bearing capacity of CHBC can be determined by Equation (9).

$$F_u = \min\left\{ \begin{array}{l} 2.796 f_t \pi d l_{lap} + \min\left\{ \begin{array}{l} f_{cc} a_h l_{lap} \sin a \cos a \\ n f_{y,v} A_{s,v} / \tan a \end{array} \right\} \\ f_u A_s \end{array} \right\} \quad (9)$$

### *5.2. Validation of the Proposed Design Equation*

Based on the proposed design equation and material test results, the predicted values of bearing capacity of CHBC have been compared to the test data as shown in Table 5 where $F_{u,exp}$ and $F_{u,pre}$ are the test data and predicted results, respectively. It shows that the prediction gives an average $F_{u,pre}/F_{u,exp}$ of 1.013 with the coefficient of variation (COV) of 0.045. In addition, the deviation of the predicted results is less than 10%. In addition, the critical head size determined from the proposed equation is equal to 6.9 times the cross-sectional area of headed bar while the test results show that the value is between six and eight times the cross-sectional area of the headed bar. In conclusion, the proposed equation predicts the test data with reasonable precision.

**Table 5.** Comparison between test data and predicted data.

| No. | Specimen ID | $F_{u,exp}$ (kN) | $F_{u,pre}$ (kN) | $F_{u,pre}/F_{u,exp}$ |
|---|---|---|---|---|
| 1 | M4-D12-6d | 53.6 | 52.1 | 0.972 |
| 2 | | 53.9 | 52.1 | 0.967 |
| 3 | | 56.2 | 52.1 | 0.927 |
| 4 | M4-D12-7.5d | 59.5 | 60.1 | 1.010 |
| 5 | | 60.0 | 60.1 | 1.002 |
| 6 | | 60.6 | 60.1 | 0.992 |
| 7 | M4-D12-9d | 61.1 | 67.0 | 1.097 |
| 8 | | 61.9 | 67.0 | 1.082 |
| 9 | | 63.1 | 67.0 | 1.062 |
| 10 | M3-D12-7.5d | 53.3 | 53.8 | 1.009 |
| 11 | | 55.2 | 53.8 | 0.975 |
| 12 | | 55.3 | 53.8 | 0.973 |
| 13 | M6-D12-7.5d | 63.4 | 66.5 | 1.049 |
| 14 | | 66.4 | 66.5 | 1.002 |
| 15 | | 67.5 | 66.5 | 0.985 |
| 16 | M8-D12-7.5d | 66.4 | 69.8 | 1.051 |
| 17 | | 66.7 | 69.8 | 1.046 |
| 18 | | 67.0 | 69.8 | 1.042 |
| Mean value | | | | 1.013 |
| Coefficient of variation (COV) | | | | 0.045 |

### *5.3. Head Thickness*

Head thickness is also a concern in the design of CHBC. Heads with inadequate thickness can yield during loading, which may impair the bearing capacity of CHBC. So, the determination of the critical value of thickness is necessary.

Providing the rigid connection between head and steel bar, the head can be modelled as a cantilever beam fixed at the steel bar. Uniform compression stress over the head is assumed and the force integrated by all the compression stresses over the head-bearing surface is equal to the design tensile strength of headed bar in this paper. It should be noted that in CHBC, the tension force is not only borne by the head, so it is for conservative and convenient purposes that the force at the head is equal to the design tensile strength of the headed bar. Actually, the force at the head is equal to $F_{h,u}$ mentioned above. The analytical model of the cantilever beam can be seen in Figure 39. Based on the bending theory of beam, the stress in the head can be determined by Equation (10).

$$\begin{aligned} q_P &= \frac{P}{{a_h}^2 - A_s} a_h = \frac{f_s A_s a_h}{{a_h}^2 - \frac{\pi d^2}{4}} = \frac{f_s \pi d^2 a_h}{4{a_h}^2 - \pi d^2} \\ \sigma_h &= \frac{M_P}{S} = \frac{q_P {a_h}^2/8}{a_h {t_h}^2/6} = \frac{3}{4} \frac{f_s \pi d^2 {a_h}^2}{{t_h}^2(4{a_h}^2 - \pi d^2)} \\ \tau_h &= \frac{3}{2} \times \frac{V_P}{A} = \frac{3}{2} \times \frac{q_P a_h/2}{a_h t_h} = \frac{3}{4} \frac{f_s \pi d^2 a_h}{t_h(4{a_h}^2 - \pi d^2)} \end{aligned} \tag{10}$$

where $\sigma_h$ and $\tau_h$ are the bending stress and shear stress of head, respectively.

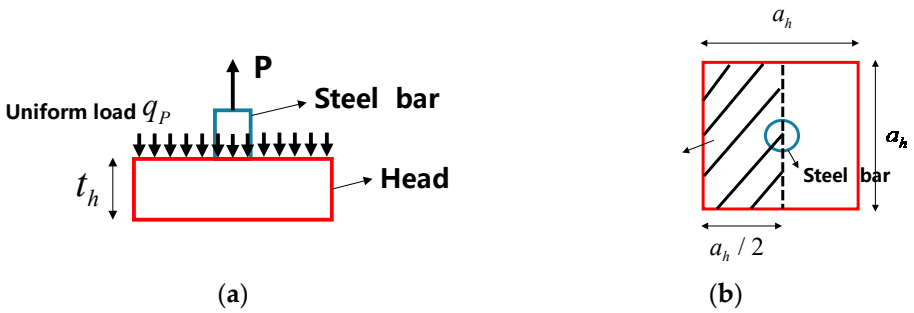


**Figure 39.** Analytical model to determine head thickness (**a**) Load on head; (**b**) Plan view of head.

So, the critical value of head thickness for yielding can be determined by Equation (11):

$$t_h = \max\left\{ \begin{array}{l} \frac{\sqrt{3}da_h}{2}\sqrt{\frac{f_s\pi}{(4{a_h}^2-\pi d^2)f_{h,y}}} \\ \frac{3\sqrt{3}}{4}\frac{f_s\pi d^2 a_h}{(4{a_h}^2-\pi d^2)f_{h,y}} \end{array} \right. \quad (11)$$

where $f_{h,y}$ is the yielding strength of head material.

Generally, welding or thread connection technique can be used to achieve the rigid connection between the head and steel bar in CHBC. The head thickness should be also in accordance with the requirements of these connection techniques.

## 6. Conclusions

In this study, the experimental investigation of 18 specimens has been conducted to study the mechanical performance of CHBC under tension. Based on the results of this study, the following conclusions are made:

(1) All the specimens of CHBC develop diagonal cracks between the heads at peak load, which are caused by the concrete compression of the diagonal strut between the heads. The confined stirrups across the diagonal cracks mainly sustain tension force and function to provide with confinement to core concrete rather than bearing shear force which can contribute to the bearing capacity of CHBC directly;

(2) For a head size equal to eight times the steel bar cross-sectional area, CHBC with only a 90 mm lap length, which is only 24% of the required lap length of straight bar splice and 36% of anchorage length of headed bar, can achieve the ultimate tensile strength of Φ12 steel bar. The CHBC can reduce the lap length of deformed bars significantly;

(3) The bearing capacity of CHBC consists of bond behavior force ($F_b$) and concrete compression force at the head ($F_h$). When the headed bar is yielding, the value of $F_b/F_h$ increases linearly with the increase in lap length and decreases with the increase in head size. In addition, the increase in lap length by 50% (increasing from 72 mm to 108 mm) can increase the value of $F_b/F_h$ by 310.0% and the increase in head size by 100% (increasing from 4 $A_s$ to 8 $A_s$) can decrease the value of $F_b/F_h$ by 20.8%. The change of $F_b/F_h$ by head size is less obvious than that of lap length;

(4) When the headed bar is yielded, under same head size, for the lap length increasing by 50% (increasing from 72 mm to 108 mm), the average bond stress is increased by 71.9% when the bond slip is increased by 48.4%. It is recommended to use small lap length in CHBC in order to reduce the slip values;

(5) Based on the superposition method and STM theory, a calculation method is proposed to determine the bearing capacity of CHBC. Compared with the test results, the deviation of predicted results is less than 10%. Moreover, the calculation of the required head thickness is suggested to prevent the head from yielding.

**Author Contributions:** Conceptualization, Z.L., C.G., S.Z., and X.L.; methodology, Z.L., S.Z., and X.L.; software, Z.L.; validation, Z.L., and S.Z.; formal analysis, Z.L., C.G. and S.Z.; investigation, Z.L.; resources, Z.L.; data curation, Z.L.; writing—original draft preparation, Z.L.; writing—review and editing, C.G. and S.Z.; visualization, Z.L.; supervision, C.G., W.L. and S.Z.; project administration, C.G., W.L. and S.Z.; funding acquisition, C.G. and W.L. All authors have read and agreed to the published version of the manuscript.

**Funding:** This study is funded by the Special Projects of Science and Technology of CHINA MINMETALS CORPORATION (2019ZXB07).

**Institutional Review Board Statement:** Ethical approval is not required.

**Informed Consent Statement:** Not applicable.

**Data Availability Statement:** All data included in this study are available upon request by contact with the corresponding author.

**Conflicts of Interest:** The authors declare no conflict of interest.

## References

1. Breccolotti, M.; Gentile, S.; Tommasini, M.; Materazzi, A.L.; Bonfigli, M.F.; Pasqualini, B.; Colone, V.; Gianesini, M. Beam-column joints in continuous RC frames: Comparison between cast-in-situ and precast solutions. *Eng. Struct.* **2016**, *127*, 129–144. [CrossRef]
2. Yee, A.A. Social Benefits and of Environmental Precast For Concrete. *PCI J.* **2001**, *46*, 14–19. [CrossRef]
3. Chang, Y.; Li, X.; Masanet, E.; Zhang, L.; Huang, Z.; Ries, R. Unlocking the green opportunity for prefabricated buildings and construction in China. *Resour. Conserv. Recycl.* **2018**, *139*, 259–261. [CrossRef]
4. Yee, A.A. Splice Sleeve for Reinforing Bars. U.S. Patent 3,540,763, 17 November 1970.
5. Lu, Z.; Huang, J.; Li, Y.; Dai, S.; Peng, Z.; Liu, X.; Zhang, M. Mechanical behaviour of grouted sleeve splice under uniaxial tensile loading. *Eng. Struct.* **2019**, *186*, 421–435. [CrossRef]
6. Liu, C.; Pan, L.; Liu, H.; Tong, H.; Yang, Y.; Chen, W. Experimental and numerical investigation on mechanical properties of grouted-sleeve splices. *Constr. Build. Mater.* **2020**, *260*, 120441. [CrossRef]
7. Yuan, H.; Zhenggeng, Z.; Naito, C.J.; Weijian, Y. Tensile behavior of half grouted sleeve connections: Experimental study and analytical modeling. *Constr. Build. Mater.* **2017**, *152*, 96–104. [CrossRef]
8. Ling, J.H.; Rahman, A.B.; Ibrahim, I.S.; Abdul Hamid, Z. Tensile capacity of grouted splice sleeves. *Eng. Struct.* **2016**, *111*, 285–296. [CrossRef]
9. Yu, Q.; Sun, J.; Xu, Z.; Li, L.; Zhang, Z.; Yu, S. Mechanical Analysis of Grouted Sleeve Lapping Connector. *Appl. Sci.* **2019**, *9*, 4867. [CrossRef]
10. Zheng, G.; Kuang, Z.; Xiao, J.; Pan, Z. Mechanical performance for defective and repaired grouted sleeve connections under uniaxial and cyclic loadings. *Constr. Build. Mater.* **2020**, *233*, 117233. [CrossRef]
11. Zhang, X.; Zhao, Y.; Guo, Y.; Li, Z. Equivalent stress-strain model of half grouted sleeve connection under monotonic and repeated loads: Experiment and preliminary application. *Eng. Struct.* **2022**, *260*, 114247. [CrossRef]
12. Liu, Q.; Lin, Y.; Li, J.; Yang, C.; Chen, J.; Zhang, M.; Liu, B. Bond strength prediction model of defective grout materials in half-grouted sleeve connections under uniaxial and cyclic loadings. *Constr. Build. Mater.* **2022**, *352*, 128981. [CrossRef]
13. Lu, Z.; Wang, Y.; Li, J.; Fan, Q. Experimental study on seismic performance of L-shaped partly precast reinforced concrete shear wall with cast-in-situ boundary elements. *Struct. Des. Tall Spec. Build.* **2019**, *28*, e1602. [CrossRef]
14. Li, J.; Fan, Q.; Lu, Z.; Wang, Y. Experimental study on seismic performance of T-shaped partly precast reinforced concrete shear wall with grouting sleeves. *Struct. Des. Tall Spec. Build.* **2019**, *28*, e1632. [CrossRef]
15. Li, J.; Wang, L.; Lu, Z.; Wang, Y. Experimental study of L-shaped precast RC shear walls with middle cast-in-situ joint. *Struct. Des. Tall Spec. Build.* **2018**, *27*, e1457. [CrossRef]
16. Xu, L.; Pan, J.; Cai, J. Seismic performance of precast RC and RC/ECC composite columns with grouted sleeve connections. *Eng. Struct.* **2019**, *188*, 104–110. [CrossRef]
17. Xu, L.; Pan, J.; Guo, L. Mechanical performance of precast RC columns with grouted sleeve connections. *Eng. Struct.* **2022**, *252*, 113654. [CrossRef]
18. Liu, H.; Chen, J.; Xu, C.; Du, X. Seismic performance of precast column connected with grouted sleeve connectors. *J. Build. Eng.* **2020**, *31*, 101410. [CrossRef]
19. Yu, J.; Zhang, E.; Xu, Z.; Guo, Z. Seismic Performance of Precast Concrete Frame Beam-Column Connections with High-Strength Bars. *Materials* **2022**, *15*, 7127. [CrossRef]
20. Hb, J.; Hs, Z.; Wq, L.; Hy, Y. Experimental study on plug-in filling hole for steel bar anchorage of the PC structure. *J. Harbin Inst. Technol.* **2011**, *43*, 28–36.
21. Chen, Z.; Wang, H.; Wang, H.; Jiang, H.; Zhu, X.; Wang, K. Application of the Hybrid Simulation Method for the Full-Scale Precast Reinforced Concrete Shear Wall Structure. *Appl. Sci.* **2018**, *8*, 252. [CrossRef]

22. Gu, Q.; Dong, G.; Wang, X.; Jiang, H.; Peng, S. Research on pseudo-static cyclic tests of precast concrete shear walls with vertical rebar lapping in grout-filled constrained hole. *Eng. Struct.* **2019**, *189*, 396–410. [CrossRef]
23. Ma, C.; Jiang, H.; Wang, Z. Experimental investigation of precast RC interior beam-column-slab joints with grouted spiral-confined lap connection. *Eng. Struct.* **2019**, *196*, 109317. [CrossRef]
24. Xu, F.; Wang, K.; Wang, S.; Li, W.; Liu, W.; Du, D. Experimental bond behavior of deformed rebars in half-grouted sleeve connections with insufficient grouting defect. *Constr. Build. Mater.* **2018**, *185*, 264–274. [CrossRef]
25. Guo, T.; Yang, J.; Wang, W.; Li, C. Experimental investigation on connection performance of fully-grouted sleeve connectors with various grouting defects. *Constr. Build. Mater.* **2022**, *327*, 126981. [CrossRef]
26. Xiao, S.; Wang, Z.; Li, X.; Harries, K.A.; Xu, Q.; Gao, R. Study of effects of sleeve grouting defects on the seismic performance of precast concrete shear walls. *Eng. Struct.* **2021**, *236*, 111833. [CrossRef]
27. Xie, L.; Wang, X.; Zhong, B.; Yang, C.; Chen, X.; Miao, Q.; Liu, Q. Full-scale experimental investigation on the seismic performance of PC columns before and after repair of grouting defects. *J. Build. Eng.* **2022**, *58*, 104996. [CrossRef]
28. Li, F.; Abruzzese, D.; Milani, G.; Li, S. Influence of internal defects of semi grouted sleeve connections on the seismic performance of precast monolithic concrete columns. *J. Build. Eng.* **2022**, *49*, 104009. [CrossRef]
29. Devries, R.A. *Anchorage of Headed Reinforcement in Concrete*; The University of Texas at Austin: Austin, TX, USA, 1996.
30. Bashandy, T.R. *Application of Headed Bar in Concrete Member*; The University of Texas at Austin: Austin, TX, USA, 1996.
31. Islam, S.; Afefy, H.M.; Sennah, K.; Azimi, H. Bond characteristics of straight- and headed-end, ribbed-surface, GFRP bars embedded in high-strength concrete. *Constr. Build. Mater.* **2015**, *83*, 283–298. [CrossRef]
32. Maranan, G.B.; Manalo, A.C.; Karunasena, W.; Benmokrane, B. Pullout behaviour of GFRP bars with anchor head in geopolymer concrete. *Compos. Struct.* **2015**, *132*, 1113–1121. [CrossRef]
33. Miao, T.; Zheng, W. Local bearing capacity of concrete under the combined action of pressure force and bond stress. *Constr. Build. Mater.* **2019**, *226*, 152–161. [CrossRef]
34. Miao, T.; Zheng, W. Distributive relationship of anchorage force relative to reinforcement and headed bars. *Eng. Struct.* **2020**, *209*, 109961. [CrossRef]
35. Yuan, L.; Yang, Y.; Sun, B.; Zhao, W. Anchorage behavior of large shear reinforcements with anchor heads and 180-degree hooks. *Structures* **2022**, *44*, 647–664. [CrossRef]
36. Singhal, S.; Chourasia, A.; Kajale, Y. Cyclic behaviour of precast reinforced concrete beam-columns connected with headed bars. *J. Build. Eng.* **2021**, *42*, 103078. [CrossRef]
37. *GB 50010-2020*; Code for Design of Concrete Structure. China Architecture and Building Press: Beijing, China, 2020.
38. *ACI318-19*; Building Code Requirements for Structural Concrete and Commentary. American Concrete Institute: Farmington Hills, MI, USA, 2019.
39. Thompson, M.; Ledesma, A.; Breen, J. Lap splices anchored by headed bars. *ACI Struct. J.* **2006**, *2*, 271–279.
40. Tarabia, A.M.; Mahmoud, Z.I.; Shoukry, M.S.; Abudina, A.A. Performance of R.C. slabs with lap splices using headed bars. *Alex. Eng. J.* **2016**, *55*, 2729–2740. [CrossRef]
41. Li, L.; Jiang, Z. Flexural Behavior and Strut-and-tie Model of Joints with headed bar details Connecting Precast Members. *Perspect. Sci.* **2016**, *7*, 253–260. [CrossRef]
42. Vella, J.P.; Vollum, R.L.; Jackson, A. Flexural behaviour of headed bar connections between precast concrete panels. *Constr. Build. Mater.* **2017**, *154*, 236–250. [CrossRef]
43. Vella, J.P.; Vollum, R.L.; Jackson, A. Investigation of headed bar joints between precast concrete panels. *Eng. Struct.* **2017**, *138*, 351–366. [CrossRef]
44. Vella, J.P.; Vollum, R.; Jackson, A. *Headed Bar Connections between Precast Concrete Panels Loaded in Bending*; Springer International Publishing: Cham, Switzerland, 2017; pp. 989–997.
45. Vieito, I.; Herrador, M.F.; Martínez-Abella, F.; Varela-Puga, F. Proposal and assessment of an efficient test configuration for studying lap splices in reinforced concrete. *Eng. Struct.* **2018**, *165*, 1–10. [CrossRef]
46. *GB/T 50081-2019*; Standard for Test Method of Mechanical Properties on Ordinary Concrete. China Architecture and Building Press: Beijing, China, 2019.
47. *GB/T 28900-2012*; Test Methods of Steel for Reinforcement of Concrete. China Architecture and Building Press: Beijing, China, 2012.
48. *GB/T 228.1-2021*; Metallic Materials-Tensile Testing-Part 1: Method of Test at Toom Temperature. General Adminstration of Quality Supervision, Inspection and Quarantine of China: Beijing, China, 2021.
49. *JGJ 355-2015*; Technical Specification for Grout Sleeve Splicing of Rebars. China Architecture and Building: Beijing, China, 2015.
50. Jun, T.; Zuo-Hua, L.; An, L.; Liang, C. A Plastic-Damage Uniaxial Compression Constitutive Model for Stirrup Confined Concrete. *Eng. Mech.* **2014**, *31*, 189–194.
51. Collins, M.P.; Mitchell, D. *Prestressed Concrete Structures*; Prentice-Hall: Englewood Cliffs, NJ, USA, 1991.

52. Mander, J.B.; Priestley, M.J.N.; Park, R. Theoretical stress strain model for confined concrete. *J. Struct. Eng.* **1988**, *114*, 1804–1826. [CrossRef]
53. Youlin, X.; Wendu, S.; Hong, W. An experiment study of bond-anchorage properties of bar in concrete. *J. Build. Struct.* **1994**, *15*, 26–37.

**Disclaimer/Publisher's Note:** The statements, opinions and data contained in all publications are solely those of the individual author(s) and contributor(s) and not of MDPI and/or the editor(s). MDPI and/or the editor(s) disclaim responsibility for any injury to people or property resulting from any ideas, methods, instructions or products referred to in the content.